

2009-01-13

Development of an optoelectronic holographic otoscope system for characterization of sound-induced displacements in tympanic membranes

Nesim Hulli

Worcester Polytechnic Institute

Follow this and additional works at: <https://digitalcommons.wpi.edu/etd-theses>

Repository Citation

Hulli, Nesim, "Development of an optoelectronic holographic otoscope system for characterization of sound-induced displacements in tympanic membranes" (2009). *Masters Theses (All Theses, All Years)*. 76.

<https://digitalcommons.wpi.edu/etd-theses/76>

This thesis is brought to you for free and open access by [Digital WPI](#). It has been accepted for inclusion in Masters Theses (All Theses, All Years) by an authorized administrator of Digital WPI. For more information, please contact wpi-etd@wpi.edu.

Development of an optoelectronic holographic otoscope system for characterization of sound-induced displacements in tympanic membranes

A Thesis
submitted to the faculty of the

Worcester Polytechnic Institute

as a partial fulfillment of the requirements for the
Degree of Master of Science
in
Mechanical Engineering

by

Nesim Hulli

15 December 2008

Approved:

Prof. Cosme Furlong, Major Advisor

Prof. Ryszard J. Pryputniewicz, Member, Thesis Committee

Prof. Glenn R. Gaudette, Member, Thesis Committee

Prof. John J. Rosowski, Mass. Eye & Ear Infirmary, Harvard-MIT Div. of Health Sciences and Technology, Member, Thesis Committee

Dr. Maria del Socorro Hernández-Montes, CIO., MX., Member, Thesis Committee

Prof. Yiming Rong, Graduate Committee Representative

Copyright © 2008

By

NEST – NanoEngineering, Science, and Technology
CHSLT – Center for Holographic Studies and Laser micro-mechaTronics
Mechanical Engineering Department
Worcester Polytechnic Institute
Worcester, MA 01609-2280

All rights reserved

ABSTRACT

The conventional methods for diagnosing pathological conditions of the tympanic membrane (TM) and other abnormalities require measuring its motion while responding to acoustic excitation. Current methodologies for characterizing the motion of the TM are usually limited to either average acoustic estimates (admittance or reflectance) or single-point mobility measurements, neither of which is sufficient to characterize the detailed mechanical response of the TM to sound. Furthermore, while acoustic and single-point measurements are useful for the diagnosis of some middle ear disorders, they are not useful in others. Measurements of the motion of the entire TM surface can provide more information than these other techniques and may be superior for the diagnosis of pathology. In this Thesis, the development of an optoelectronic holographic otoscope (OEHO) system for characterization of nanometer scale motions in TMs is presented. The OEHO system can provide full-field-of-view information of the sound-induced displacements of the entire surface of the TM at video rates, allowing rapid quantitative analysis of the mechanical response of normal or pathological TMs.

Preliminary measurements of TM motion in cadaveric animals helped constrain the optical design parameters for the OEHO, including the following: image contrast, resolution, depth of field (*DOF*), laser power, working distance between the interferometer and TM, magnification, and field of view (*FOV*). Specialized imaging software was used in selecting and synthesizing the various components. Several prototypes were constructed and characterized. The present configuration has a resolution of 57.0 line pairs/mm, *DOF* of 5 mm, *FOV* of $10 \times 10 \text{ mm}^2$, and a 473 nm laser with illumination power of 15 mW.

The OEHO system includes a computer controlled digital camera, a fiber optic subsystem for transmission and modulation of laser light, and an optomechanical system for illumination and observation of the TM. The OEHO system is capable of operating in two modes. A 'time-averaged' mode, processed at video rates, was used to characterize the frequency dependence of TM displacements as tone frequency was swept from 500 Hz to 25 kHz. A 'double-exposure' mode was used at selected frequencies to measure, in full-field-of-view, displacements of the TM surface with nanometer resolution.

The OEHO system has been designed, fabricated, and evaluated, and is currently being evaluated in a medical-research environment to address basic science questions regarding TM function. Representative time-averaged holographic and stroboscopic interferometry results in post-mortem and live samples are herein shown, and the potential utilization discussed.

This thesis is dedicated proudly to my family.

ACKNOWLEDGEMENTS

At this time, it is extremely important to extend my gratitude to a number of individuals and organizations which have aided me and made it possible for me to arrive at this moment with these results.

Most important, I'm very grateful for all the support and friendship which were offered to me by my advisor Professor Cosme Furlong, whom I shall never forget. I thank Professor Ryszard Pryputniewicz for offering me the opportunity to study interferometry and MEMS systems during my time at WPI. These professors and my committee have demonstrated unwavering support during my Thesis research. The Center for Holographic Studies and Laser micromechaTronics (CHSLT) in the WPI Mechanical Engineering Department, for the use of both their facilities and equipment, deserve much praise and recognition.

I wish to acknowledge the assistance of Professor John J. Rosowski and Dr Jeffrey T. Cheng for their collaboration, advice and suggestions in my experimental work. Funding and support from Dr. Saumil Merchant and his generous patients at Massachusetts Eye and Ear Infirmary were extremely important in the project as well.

Accolades are also extended to Dr. Maria del Socorro Hernandez-Montes, Ellery Harrington, and Haiyang Yang and from the CHSLT laboratories for their enduring support and invaluable assistance.

Finally, I want to thank my dear family for their love and unending support during my work over the past couple of years and more. Without them I would not have been able to accomplish anything.

TABLE OF CONTENTS

Copyright	i
Abstract	ii
Acknowledgements	v
Table of contents	vi
List of figures	viii
List of tables	xi
Nomenclature	xii
Objective	xvi
1. Introduction	1
2. Background	4
2.1. Anatomy of the ear	4
2.1.1. The tympanic membrane	6
2.1.2. Medical techniques and procedures for diagnosis	7
3. Theory of interferometry	11
3.1. Fundamentals of interferometry	11
3.1.1. Electromagnetic wave propagation	12
3.1.2. The sensitivity vector, the fringe locus function and the displacement vector	14
3.1.3. Double-exposure holography	17
3.1.4. Time-averaged holography	19
4. Implementation of optoelectronic holographic otoscope system	23
4.1. Fiber optic subsystem	24

4.2. Otoscope head subsystem	25
5. Evaluation of the optoelectronic holographic otoscope system	39
5.1. Analytical results	41
5.2. Computational results	44
5.3. Results comparisons	46
6. Optoelectronic holographic otoscope system in medical environment	49
6.1. Experimental results in tympanic membrane	50
7. Conclusions and future work	60
8. References	62
Appendix A. MATLAB code for line profile contrast calculation	69
Appendix B. Mathcad file for determining the sensitivity vector for OEHO system	72

LIST OF FIGURES

Fig.	2.1.	Anatomy of the human ear: The cross section of human ear showing divisions of the outer, middle, and inner ears [Wikipedia, 2008].	5
Fig.	2.2.	Middle ear ossicles: (a) chain of ossicles and their ligaments, (b) the three bones: malleus (M) incus (I) and stapes (S) [Csillag, 2005].	5
Fig.	2.3.	Structure of the human tympanic membrane: (a) normal tympanic membrane as seen through an otoscope [Grundman et al., 2008], (b) schematic of a right tympanic membrane [Sundberg, 2008].	6
Fig.	2.4.	The tympanometer consists of a hand-held probe to be inserted into the ear. The probe is composed of three tubes containing a loudspeaker, a microphone and a pump [Mikoklai et al., 2008].	8
Fig.	3.1.	Electromagnetic wave propagation composed of perpendicular electric and magnetic fields in the x-y plane.	12
Fig.	3.2.	Illumination and observation geometry for holographic interferometry: R_p , R_1 , and R_2 are the position vectors whereas \mathbf{K}_1 and \mathbf{K}_2 are the illumination and the observation vectors, respectively. \mathbf{K} is the sensitivity vector.	14
Fig.	4.1.	Schematic of the OEHO system: TM is the sample under investigation; OH is the otoscope head containing an interferometer and imaging optics; FS is the fiber optic subsystem containing a laser, beam splitting optics, and laser-to-fiber components to provide an object beam (OB) and reference beam (RB); OH and FS are controlled by the image processing computer (IP). SS is the integrated sound source, and MP is the microphone. FG is the frequency generator which provides the timing input to the AOM driver (AOMD).	23

Fig.	4.2.	Fiber optic subsystem: (a) schematic model depicting the major components; (b) CAD model depicting the major components; and (c) fabricated subsystem.	24
Fig.	4.3.	Ray tracing using commercially available software. <i>S_o</i> : Object to front principal point distance, <i>S_i</i> : Rear principal point to image distance, <i>DOF</i> : Depth of field.	26
Fig.	4.4.	Diagram of the imaging system: (a) parameters of the imaging system taken into account for the optical design. <i>FOV</i> : Field of view, <i>f</i> : Focal length, <i>ROI</i> : Region of interest, (b) target <i>FOV</i> of 10x10 mm ² .	28
Fig.	4.5.	MTF evaluated from OSLO software.	30
Fig.	4.6.	Otoscope head subsystem: (a) schematic model depicting the major components; (b) CAD models depicting the major components; and (c) fabricated subsystem.	33
Fig.	4.7.	USAF 1951 positive and negative target pattern [Edmund Optics, Inc., 2006].	34
Fig.	4.8.	Specification table for the USAF resolution target [Edmund Optics, Inc., 2006].	35
Fig.	4.9.	Recorded USAF 1951 negative glass target with group 5 outlined for containing the smallest resolvable element set [Edmund Optics, Inc., 2006].	36
Fig.	4.10.	Line profile contrast calculation method (a) image of G4E2 showing a line profile, (b) line intensity profile and contrast calculation.	37
Fig.	5.1.	A coated copper foil mounted on to the piezoelectric shaker.	39
Fig.	5.2.	Time-averaged interferograms of a test copper sample.	41
Fig.	5.3.	First mode of vibration obtained with MathCAD [Dwyer et al., 2008].	44
Fig.	5.4.	Finite element method results for natural frequencies of a test copper sample [Dwyer et al., 2008].	45
Fig.	6.1.	OEHO system installation: (a) OEHO system at MEEI; (b) otoscope head subsystem testing post mortem	49

	human temporal bone at MEEI; and (c) otoscope head subsystem testing post mortem chinchilla at MEEI.	
Fig. 6.2.	Time-averaged holograms measured in cadaveric humans, in cadaveric chinchilla, in live chinchilla, and in cadaveric cat. The schematic on the top row shows the area of the TM in gray, location of the malleus, the umbo and the probe tube.	51
Fig. 6.3.	Synchronization of the illumination with the object excitation.	52
Fig. 6.4.	Full-field-of-view stroboscopic holography measurements in human temporal bone at 500 Hz, showing a peak-to-peak surface out of plane displacement on the order of 90nm: (a) unwrapped phase (2D plot); and (b) 3D plot.	54
Fig. 6.5.	Full-field-of-view stroboscopic holography measurements in human temporal bone at 800 Hz, showing a peak-to-peak surface out of plane displacement on the order of 120nm: (a) unwrapped phase (2D plot); and (b) 3D plot.	55
Fig. 6.6.	Full-field-of-view stroboscopic holography measurements in human temporal bone at 4 kHz, showing a peak-to-peak surface out of plane displacement on the order of 190nm: (a) unwrapped phase (2D plot); and (b) 3D plot.	56
Fig. 6.7.	Full-field-of-view stroboscopic holography measurements in human temporal bone at 12 kHz, showing a peak-to-peak surface out of plane displacement on the order of 150nm: (a) unwrapped phase (2D plot); and (b) 3D plot.	57
Fig. 6.8.	Full-field-of-view stroboscopic holography measurements in human temporal bone at 15 kHz, showing a peak-to-peak surface out of plane displacement on the order of 210nm: (a) unwrapped phase (2D plot); and (b) 3D plot.	58
Fig. 6.9.	Full-field-of-view stroboscopic holography measurements in human temporal bone at 20 kHz, showing a peak-to-peak surface out of plane displacement on the order of 60nm: (a) unwrapped phase (2D plot); and (b) 3D plot.	59

LIST OF TABLES

Table 4.1.	Lenses tested.	28
Table 4.2.	Working distance constraints.	38
Table 5.1.	Membrane test data.	40
Table 5.2.	First six mode shapes and frequencies provided with ACES methodology [Dwyer et al., 2008].	46
Table 5.3.	Experimental result percent error [Dwyer et al., 2008].	48

NOMENCLATURE

$ $	magnitude
(x, y)	coordinates
$\Delta\phi$	random phase difference between ϕ_o and ϕ_r
$\Delta\theta$	known phase step introduced between the frames
Δt	exposure of the camera
ϵ	electric permittivity of the medium
θ	angle of incidence
θ_n	phase step
λ	laser wavelength
v	wave propagation velocity
\emptyset	relative phase between two waves
ϕ_o	randomly varying phase of the object beam
ϕ_r	phase of the reference beam
ω	circular frequency
Ω	fringe locus function
Ω_t	time varying fringe locus function
f	focal length
k	wave number, $\frac{2\pi}{\lambda}$
\mathbf{k}	elastic modulus of the plate
l_l	line length
m	the rank of the root
n	the order of the root
\mathbf{n}	fringe order number
$n(x, y)$	fringe order number at known (x, y)
ps_{CCD}	pixel size of the CCD
t	time

A_1, A_2	vector amplitudes
A_n, B_n, C_n, D_n	the coefficients used to determine the mode shapes
A_o	amplitude of an object beam
A_r	amplitude of a reference beam
B	magnetic field
Br	beam ratio
C	contrast
D	flexural rigidity of the plate
D_a	aperture diameter
D_l	lens diameter
DOF	depth of field
E	electric field
E_1, E_2	electric field vectors
$F/\#$	f number
E_o, E_r	complex light fields
FOV	field of view
I	intensity
I_{max}	the maximum interferogram intensity
I_{min}	the minimum interferogram intensity
I_n	phase stepped intensity
I_n'	intensity of the deformed object
I_o	intensity of the object beam
I_r	intensity of the reference beam
$I_{t_n}(x, y)$	intensity distribution of the n -th frame where $n = 4$
J_n	Bessel functions of the first kind
J_o	zero order Bessel function of the first kind
\mathbf{K}	sensitivity vector

\mathbf{K}_1	illumination vector
K_{1x}, K_{1y}, K_{1z}	Cartesian components of the illumination vector
\mathbf{K}_2	observation vector
K_{2x}, K_{2y}, K_{2z}	Cartesian components of the observation vector
K_n	the modified Bessel functions of the second kind
\mathbf{L}	displacement vector
M	characteristic function
MAG	magnification
NA	numerical aperture
ROI	region of interest
R_p, R_1, R_2, R_n	position vectors where $n = 1, 2, \mathbf{P}$
R_x, R_y, R_z	Cartesian components of the position vectors
S_i	image distance
S_o	object distance
W	deformation of the plate
Y_n	Bessel functions of the second kind
Z_n	the modified Bessel functions of the second kind
ACES	analytical, computational, and experimental solutions
AOM	acousto-optic modulator
AOMD	acousto-optic modulator driver
BS	beam splitter
BSI	imaging beam splitter
CCD	charge-coupled device
FA	laser-to-fiber coupler assemblies
FEM	finite element method
FG	frequency generator
FS	fiber optic subsystem

I	incus
IS	imaging system
IS	illumination source
IP	image processing computer
LD	laser
LDV	laser doppler vibrometry
M	mirror
M	malleus
MEMS	microelectromechanical systems
MP	microphone
MPM	mirror mounted onto piezoelectric modulator
MTF	modulation transfer function
O	observation source
OB	object beam
OEHO	optoelectronic holographic otoscope
OH	otoscope head
P	random point on the object
P_i	principal inertia of the plate
RB	reference beam
R_i	rotary inertia of the plate
S	speculum
S	stapes
SLV	scanning laser vibrometer
SS	sound source
TM	tympanic membrane

OBJECTIVE

The objective of this Thesis is the development of a compact, full-field-of-view optoelectronic, high-speed measurement system for otology applications. The measurement system is based on an optoelectronic holographic otoscope (OEHO) which enables measurements of shape and deformations of nanometer scale resolution in tympanic membranes (TMs). This Thesis will demonstrate the effectiveness of the OEHO; validate the optomechanical design and the measurements provided by the OEHO, and present new data for different species.

1. INTRODUCTION

Recent advances in medical technology have given medical professionals increasingly accurate tools. In all aspects of the medical fields, sophisticated equipment is being used for everything from making diagnoses to performing surgeries. Currently, knowledge of both the functionality of the middle ear and related hearing conditions is expanding as a result of these new technologies. In particular, the tympanic membrane (TM) is being examined more quantitatively than ever before.

The TM, which plays an important role in the transmission of sound into the cochlea, is a tissue separating the external ear canal from the middle ear cavity [Rosowski, 1996]. Experimental measurements and theoretical analysis have been done to study the structure [Lim, 1970, 1995], mechanical properties [Funnel and Laszlo, 1978; Fay et al., 2005] and acoustic function [Tonndorf and Khanna, 1970; Rosowski et al., 1986] of the TM.

The efficiency of sound coupling through the TM can be hindered by changes to the TM through trauma or middle-ear diseases. By measuring the deformation of the TM with various acoustic stimuli, the degree of hearing loss can be determined.

Most present day middle ear diagnostic procedures are based on acoustic measurements that sense the mobility of the entire TM, e.g., multi or single frequency tympanometry [Shanks et al., 1988; Margolis et al., 1999], ear canal reflectance or power absorption [Keefe et al., 1993; Feeney et al., 2003; Allen et al., 2005], and static pressure induced variations in sound pressure [Wada et al., 1989]. However, single-point laser vibrometer measurements of the mobility of the umbo in the TM

have also been used as diagnostic aids in the clinic [Huber et al., 2001; Whittemore et al., 2004; Rosowski et al., 2008].

All of these clinic measurements have weaknesses. The acoustic measurements depend on the sound pressure at the TM and represent the average mobility of the entire TM. The single-point laser vibrometry measurements are much more localized, which may lead to a superior ability to distinguish ossicular disorders [Rosowski et al., 2008], but are relatively insensitive to TM disorders at locations other than the umbo. Full-field-of-view measurements of the TM mobility may be superior to either of the present techniques in that they will quantify the motion of the entire surface of the TM. Optoelectronic holography, which has been successfully tested in many applications and environments, [Pryputniewicz et al., 2002] in this regard has shown the capability to provide the desired information on the state of the tympanic membrane.

Holographic methodologies have been used in the past to enable full-field-of-view measurements of the vibrating patterns of the surface of the TMs, but there are only a few holographic studies, which describe the motion of the entire mammalian TM within a limited frequency range (0.1 ~ 8 kHz) [Wada et al., 2002; Khanna and Tonndorf, 1972; Tonndorf and Khanna, 1971].

Currently, the most detailed description of the motion of the TM comes from time-averaged holograms measured in animals [Khanna and Tonndorf, 1972] and human cadavers [Tonndorf and Khanna, 1972]. These data provide good qualitative descriptions of the magnitude of sound-induced motions of the TM surface. However, the published data using these techniques are few. Therefore, some fundamental questions of TM functions have not been answered.

In this Thesis, the sound-induced motion of the TM surface in postmortem preparations from three mammalian species: cat, chinchilla (including one live chinchilla) and human cadavers, were measured using an optoelectronic holographic otoscope (OEHO) system.

The OEHO system, which is designed for fields-of-view on the order of 10 mm in diameter, uses a solid state laser (wavelength $\lambda = 473$ nm) and is operated in two modes. The ‘time-averaged’ holography mode is used for rapid identification of resonant frequencies and corresponding mode shapes of vibration of samples [Furlong and Pryputniewicz, 1996]. The ‘double-exposure’ mode is used for determination of the magnitude and phase of displacements over the entire TM surface with nanometer resolution [Furlong et al., 2007].

As with the development of any system, at some point it becomes necessary to demonstrate its integrity. An understood geometry with characteristics or qualities that were predictable was necessary to compare and draw conclusions with the experimental results that could be derived. Because tympanic membrane geometry is complex, the performance of the system was evaluated with a simplified circular plate employing finite element and analytical methods, as well as experimental data.

Additionally, described herein are the advances in the design, fabrication, characterization, and use of a compact, stable OEHO system currently in use in medical research environments.

2. BACKGROUND

2.1. Anatomy of the ear

Anatomically, the mammalian ear can be divided into three functional parts as shown in Fig. 2.1: the outer (external) ear, the middle ear and the inner ear. The external ear which consists of auricle or pinna (the visible part of the ear) and the external auditory canal collects sound waves and transmits them to the middle ear.

The middle ear is a space filled with air that encapsulates the three middle ear bones (ossicles) and the middle ear muscles as presented in Fig. 2.2. The first bone, the hammer (malleus), is connected to the anvil (incus), which in turn is connected to the stirrup (stapes). The middle ear is attached to the back of the nose (nasopharynx) by the Eustachian tube. In the same way that the outer ear is an apparatus of hearing, so is the middle ear. Namely, the sound energy coming from the outer ear causes the TM to vibrate. The tympanic membrane transforms acoustic energy to mechanical energy in the form of ossicular motion. The stapes converts mechanical energy to acoustic energy within the inner ear.

The inner ear contains the semicircular canals, the vestibule for balance, and the cochlea for hearing. The inner ear is where “hearing” actually takes place. Signals sent from outside are received by the inner ear, which then interacts neurologically with the brain via the vibration of microscopic ‘hairs’ (the stereocilia) with varied lengths that are attached to sensory cells. The ‘hair cells’ are arranged in an orderly fashion along the length of the auditory inner ear, where those that respond to lower frequencies are farther from the stapes. This tonotopic mapping allows the coding of sound frequency and the perception of pitch.

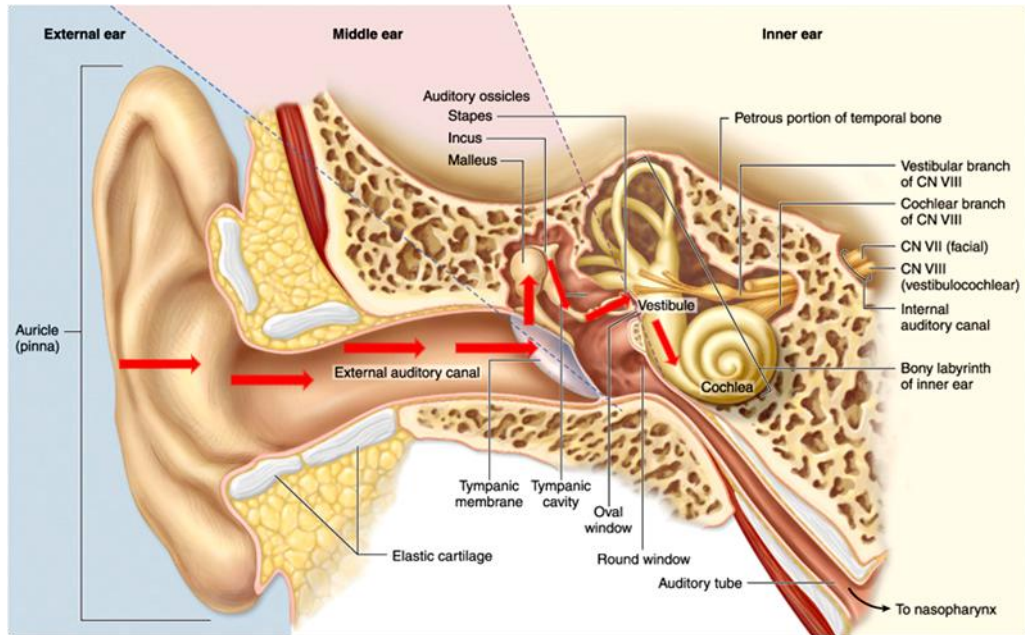


Fig. 2.1. Anatomy of the human ear: The cross section of human ear showing divisions of the outer, middle, and inner ears [Wikipedia, 2008].

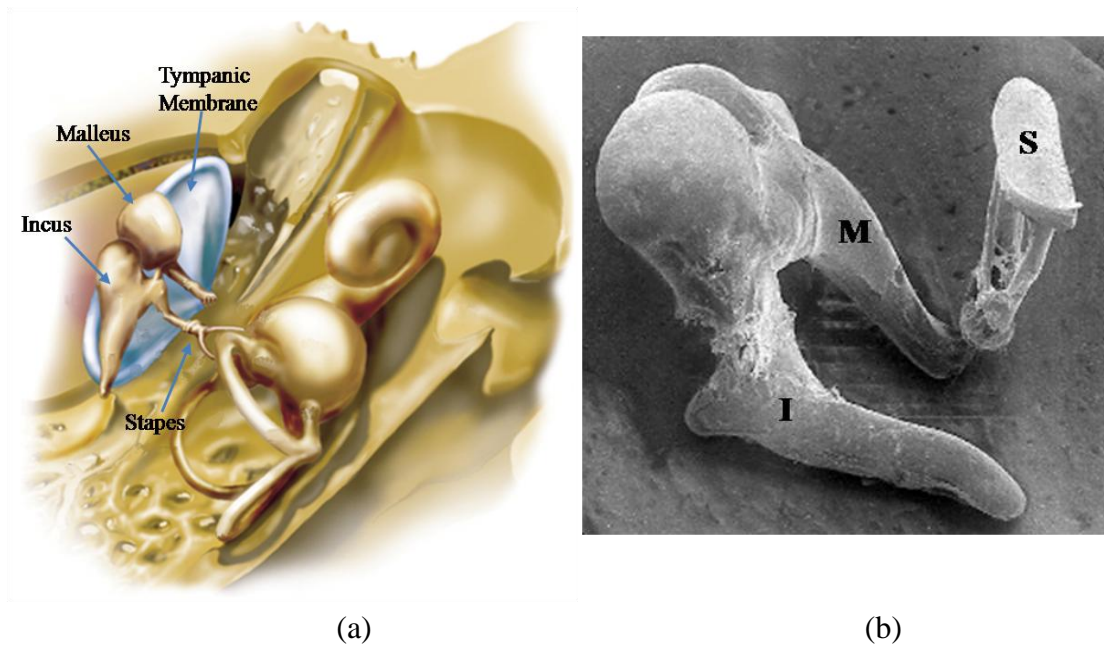


Fig. 2.2. Middle ear ossicles: (a) chain of ossicles and their ligaments, (b) the three bones: malleus (M) incus (I) and stapes (S) [Csillag, 2005].

2.1.1. The tympanic membrane

The tympanic membrane is a semi-transparent, thin, cone shaped membrane which is the boundary between the outer and middle ears, as presented in Fig. 2.3.

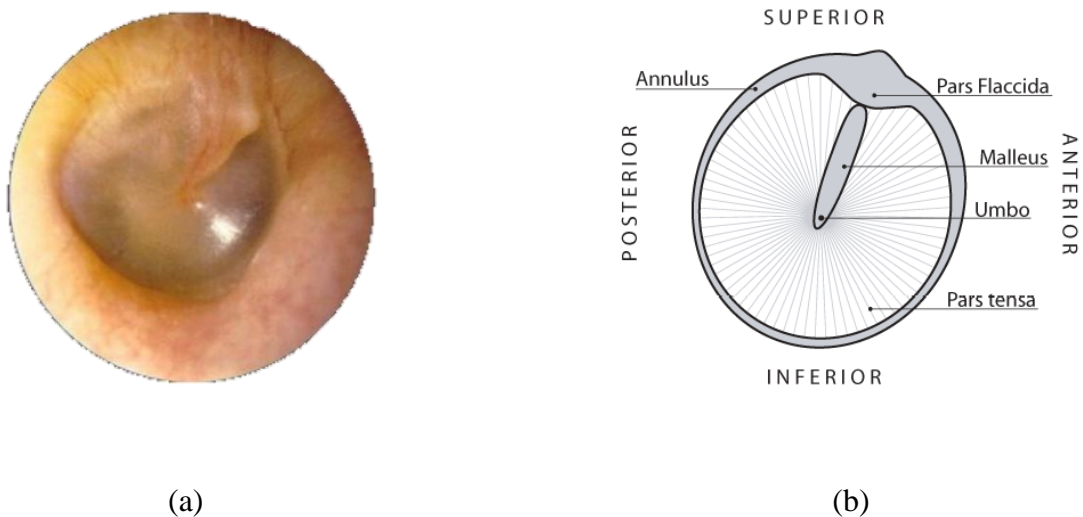


Fig. 2.3. Structure of the human tympanic membrane: (a) normal tympanic membrane as seen through an otoscope [Grundman et al., 2008], (b) schematic of a right tympanic membrane [Sundberg, 2008].

The TM is composed, structurally, of three layers. The lateral (or outside) layer is a skin-like epidermis, the medial (or inside) layer is mucosal lining much like the lining of the mouth and nose. In between is a fiber rich connective layer, called the lamina propria [Sanna et al., 2003]. The diameter of the TM is 5-10 mm, and the depth of cone is about 1.5mm [Dirckx and Decraemer, 2000]. The exterior edge of the TM, named the annulus, or the annular ring, consists of a fibrous and cartilaginous tissue that is both thicker and stiffer than the rest of the membrane [Sundberg, 2008]. The TM is between 55 and 140 micrometers thick [Kuypers et al., 2006]; it is thinnest

in the central parts of the posterosuperior quadrant and thickest in the vicinity of the inferior part of the annulus. The triangular extension at the superior part of the TM is the flexible *pars flaccida*. The *flaccida* is about 10% of the area of the TM, and moves independently from the balance of the TM area, the *pars tensa*, that is tightly coupled to the ossicular chain [Sundberg, 2008].

Since TM has unique anatomical and physical features that are ideally suited for the sound transmission in varying frequency ranges, it plays an important role in the diagnosis of middle ear disorders.

2.1.2. Medical techniques and procedures for diagnosis

To diagnose any unhealthy conditions of the middle ear, there are a limited number of different methods practiced. Developed by clinicians, tympanometry, Fig. 2.4, is a measure of the mobility of the TM and middle ear and depends on the status of the TM, the middle-ear air space and the ossicular chain [Schubert, 1980; Mikoklai et al., 2008]. Tympanometry is routinely used to help detect the presence of fluid in the middle-ear and TM perforations, but is less useful in the diagnosis of ossicular disorders.

Graphical representation of the relationship between air pressure in the external canal to the impedance of the tympanic membrane and the middle ear system can be supplied by tympanometry [Mikoklai et al., 2008]. In effect, impedance is inversely related to the mobility of the tympanic membrane; this is in actuality what physicians are testing when they determine the health of a patient's tympanic membrane [Schubert, 1980]. The physics of transmitting sound is much like what happens when

a drum is struck: part of the sound is reflected while the other part is absorbed by the instrument itself.

Likewise, when the tympanic membrane is hit by a sound, some of the sound waves are absorbed and sent to the inner ear by the ossicles, while the remaining part of the sound is reflected back.

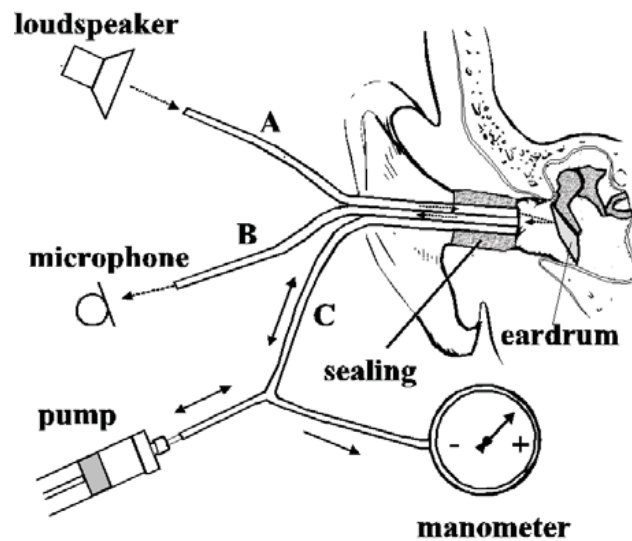


Fig. 2.4. The tympanometer consists of a hand-held probe to be inserted into the ear. The probe is composed of three tubes containing a loudspeaker, a microphone, and a pump [Mikoklai et al., 2008].

Abnormal TM mobility is an indication of a ‘conductive’ hearing loss: a problem with how sound is conducted to the inner ear sensory mechanism. A ‘sensory’ or ‘neural’ hearing loss describes a pathology associated with the conversion of sound energy into electrical energy within the hair cells and the conduction of these electrical sensory signals to the brain. The sensory or neural hearing losses are differentiated from conductive pathologies via the use of

‘bone-conduction’ hearing test. In bone-conduction testing, sound is presented to the inner ear via a mechanical vibrator placed firmly on the skull. The bone-conducted sound is thought to bypass the middle ear and stimulate the inner-ear directly. A person with a loss of sensitivity to air-conducted sound and normal sensitivity to bone-conducted sound is thought to have a ‘conductive’ hearing loss related to either middle or external-ear pathology.

Physicians induce different pressures in the ear canal and take measurements with relation to available volumes (fluid in the cochlea) [Schubert, 1980]. If the recorded volumes are found to be different from that of the normal ear, then it is very likely that there is a problem in the middle ear [Schubert, 1980]. The type of pattern detected can also help to determine what type of middle ear condition the patient has, enabling physicians to begin determining the method of treatment [Katz, 1994]. This type of analysis, together with the use of an otoscope, provides the information necessary to make proper diagnoses of specific ear ailments [Katz, 1994]. This type of testing requires various kinds of expertise and a large commitment of time.

A non contact system that uses Laser Doppler Vibrometers (LDV) to map tympanic response is the newest experimental method to test the tympanic membrane. First, the device ascertains and reports the velocity of surfaces in a system and then extracts relevant data for use by audiologists [Rosowski et al., 2008; Castellini et al., 2006]. These measurements have been demonstrated to be sensitive to several middle-ear pathologies including TM perforations and ossicular fixations and interruptions. When applied to a sample, the LDV supplies point-by-point information [Rosowski et al., 2008]. LDV can be used to measure vibrations in order

to collect multiple data points at a time and receive a magnified “field-of-view” of their data.

Used in combination with a Scanning Laser Vibrometer (SLV) to collect data from multiple points on a sample simultaneously, points within a minute area for example, to provide the whole image of the sample’s response [Castellini, et al., 1998].

There are other methods that have the capability to provide data on the TM response to be used for further analysis. Holographic interferometry, as a hybrid optical testing method, is helpful in analysis of sample deformation in full-field-of-view [Furlong and Pryputniewicz, 1998; Furlong et al., 2002; Furlong et al., 2008; Hulli et al., 2007; Hernández-Montes et al., 2008]. It must be remembered that single point measurements are not sufficient to characterize the motion of the entire TM. Special analysis equipment is required for full-field-of-view measurement methodologies of nanometer resolution if comprehensive data about the tympanic membrane is to be provided.

Optoelectronic holographic interferometry is one of the current areas of laser-related research capable of providing physicians with desired information on the condition of tympanic membranes. Theoretical aspects of interferometry will be addressed in the next section.

3. THEORY OF INTERFEROMETRY

3.1. Fundamentals of interferometry

Interferometry is a non-contact metrology technique that is capable of measuring absolute shape and deformation based on the interference of the light. Two waves of identical origin create interference patterns at the observer (bright and dark fringes) by following optical paths of different lengths, a result of the changing distance to the object's surface. Each fringe corresponds to a distance change equal to one half the wavelength of the light [Kreis, 2005].

However, the coherence and monochromaticity of light sources used in standard interferometers prior to 1960 were poor [Pryputniewicz, 1996]. As a result, classical interferometry was limited to measurements of small path-length differences of optically polished and reflecting flat surfaces [Pryputniewicz, 1996].

In the early 1960's, with the advent of light amplification by stimulated emission of radiation (laser), holography permitted interferometry to overcome this shortcoming without any alterations of the fundamental principles. The technique, based on the ability of a hologram to record the phase and amplitude of any wave, was developed by Stetson and Powell, and is known as holographic interferometry [Holophile, Inc., 2008].

Holographic interferometry revolutionized nondestructive evaluation techniques and went on to become one of the major achievements in optics at the turn of the last century [Kreis, 2005]. Holographic interferometry demands that the same medium be used to record an object from different positions. The interference of the reconstruction from multiple exposures of the object is created by the diffraction patterns; these produce fringe patterns on the reconstructed surface, which indicate the

movement of the object during the test period. The interferometric procedure has a measurement range that depends on the number of fringes that can be resolved by the CCD camera. Using a high resolution CCD camera, and a highly reflective object, out-of-plane measurements can have a range of approximately 0 to 50 μm , with a resolution on the order of a few nanometers or better [Kreis, 2005].

The basis of holographic interferometry, that is, the theories of wave propagation and interference, can be explained vis a vis holographic interferometry. It is vital that the basic element of electromagnetic wave propagation and interference be understood before presenting the theoretical aspects of hologram interferometry. This will be addressed now.

3.1.1. Electromagnetic wave propagation

The study of the interaction of light waves as they intersect one another in some medium comprises the foundation of optical interferometry [Hecht, 1989]. Light is an electromagnetic wave which can be explained in terms of an electric field component (E) and a magnetic field component (B). These two fields are perpendicular to each other, and the composed wave of E and B travels in the direction of $E \times B$ as it can be seen in Fig. 3.1

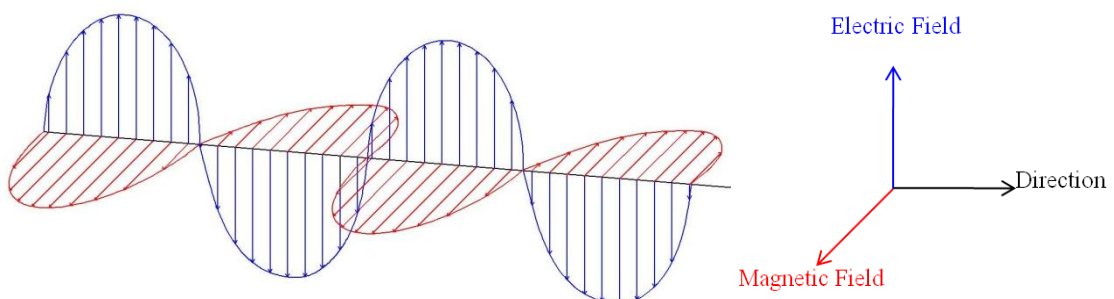


Fig. 3.1. Electromagnetic wave propagation composed of perpendicular electric and magnetic fields in the x-y plane.

In holography, the devices used to record images are only sensitive to the electric field component. In fact, it is the time-averaged intensity of the electric field squared which is detected [Robinson and Reid, 1993; Vest, 1979].

From the Maxwell equations we get the intensity as

$$I = \epsilon v \langle E^2 \rangle, \quad (3.1)$$

where I is the intensity, ϵ is the electric permittivity of the medium in which the wave propagates at velocity v and E^2 is the time-average of the electric field squared. Thus we only use proportionality between the square of the electric field and the intensity

$$I \propto \langle E^2 \rangle. \quad (3.2)$$

Interference is the combination of two or more coherent light waves emitted by the same source, which differ in the direction to form a resultant wave. Light waves are subject to the superposition principle. For example if two waves overlap the resulting fields is the vector sum of the two original fields,

$$E = E_1 + E_2. \quad (3.3)$$

The corresponding intensity due to these fields is then

$$I = \langle E^2 \rangle = \langle E_1^2 \rangle + \langle E_2^2 \rangle + 2 \cdot \langle E_1 \cdot E_2 \rangle. \quad (3.4)$$

For simplicity let's assume that both waves are linearly polarized in the same direction. The equations for the electric field vectors E_1 and E_2 can be written respectively as,

$$E_1 = A_1 \cos[\omega t - k_1 \cdot r], \quad (3.5)$$

and

$$E_2 = A_2 \cos[\omega t - k_2 \cdot r + \phi] \quad (3.6)$$

where A_1 and A_2 are the vector amplitudes, ω is its circular carrier frequency, t is the time, k is the wave number ($\frac{2\cdot\pi}{\lambda}$), and \emptyset is the relative phase between two waves.

Finally, combining equations 3.4, 3.5, and 3.6 the intensity of two overlapping electric fields can be found to be

$$I = A_1^2 + A_2^2 + 2A_1A_2 \cos[k_2 \cdot r - k_1 \cdot r - \emptyset]. \quad (3.7)$$

3.1.2. The sensitivity vector, the fringe-locus function, and the displacement vector

In addition to the description of the light fields, there are also three other quantities: the sensitivity vector, the displacement vector and the fringe locus function, which are important due to the quantitative analysis of holographic interferometry [Pryputniewicz, 1994-a, 1996; Pryputniewicz and Stetson, 1980]. The nature of the sensitivity vectors can be described with the help of Fig. 3.2, which shows the illumination \mathbf{K}_1 and the observation \mathbf{K}_2 vectors of a random test object.

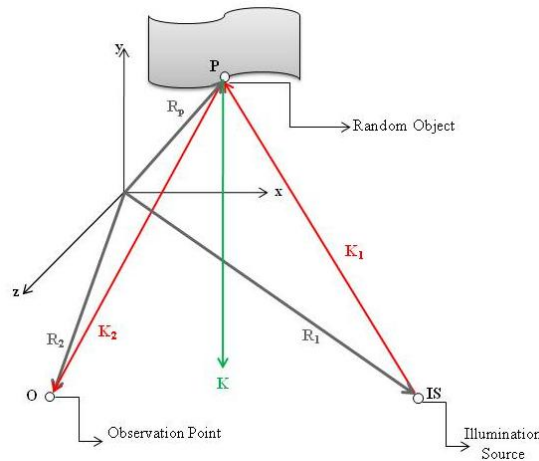


Fig. 3.2. Illumination and observation geometry for holographic interferometry: R_p , R_1 , and R_2 are the position vectors whereas \mathbf{K}_1 and \mathbf{K}_2 are the illumination and the observation vectors, respectively. \mathbf{K} is the sensitivity vector.

In Fig 3.2, **IS** illustrates the illumination source, e.g. laser, **O** is the observation point, e.g. camera, detector, or simply an eye, and **P** is an randomly selected point on the sample, where R_1 , R_2 and R_p are the position vectors which describe the spatial coordinates of these points.

These position vectors are described as

$$R_n = R_{nx}\hat{i} + R_{ny}\hat{j} + R_{nz}\hat{k} \quad n = 1,2, \mathbf{P} \quad (3.8)$$

where R_x , R_y , and R_z are the Cartesian components of these vectors.

The illumination and observation vectors \mathbf{K}_1 and \mathbf{K}_2 can be written respectively in Cartesian components as,

$$\mathbf{K}_1 = K_{1x}\hat{i} + K_{1y}\hat{j} + K_{1z}\hat{k} \quad (3.9)$$

and

$$\mathbf{K}_2 = K_{2x}\hat{i} + K_{2y}\hat{j} + K_{2z}\hat{k}. \quad (3.10)$$

Correspondingly they can be expressed in terms of the position vectors depicted in Eq. 3.8 as

$$\mathbf{K}_1 = k \frac{R_p - R_1}{|R_p - R_1|}, \quad (3.11)$$

and

$$\mathbf{K}_2 = k \frac{R_2 - R_p}{|R_2 - R_p|}. \quad (3.12)$$

In the above equations $|\quad|$ indicates a magnitude of the quantity between the vertical bars, k is the magnitude of the propagation vectors \mathbf{K}_1 and \mathbf{K}_2 , and it is related to the wavelength (λ) of the laser light

$$|\mathbf{K}_1| = |\mathbf{K}_2| = k = \frac{2\pi}{\lambda}. \quad (3.13)$$

Based on the results from Eqs 3.11 and 3.12, the sensitivity vector \mathbf{K} , which specifies the direction of deformation to which a holographic setup will be most sensitive, can be calculated (Appendix B) as the difference between the observation vector \mathbf{K}_1 , and the illumination vector \mathbf{K}_2 ,

$$\mathbf{K} = \mathbf{K}_2 - \mathbf{K}_1. \quad (3.14)$$

The methods of holographic interferometry allow measurement range of object displacements from a hundredth to several hundreds of a wavelength [Kreis, 2005; Vest, 1979].

As an object deforms or is displaced during the recording of a hologram, the optical path length of the light reflected off the object changes. These results in phase differences are recorded in the form of fringes. These fringes are described by a fringe-locus function (Ω) constant values of which define fringe loci on the object's surface. The fringe-locus function relates directly to the fringe orders (\mathbf{n})

$$\Omega = 2\pi\mathbf{n}. \quad (3.15)$$

Additionally, the fringe-locus function can be related to the scalar product of the sensitivity vector \mathbf{K} with the displacement vector \mathbf{L} as

$$\Omega = \mathbf{K} \cdot \mathbf{L}. \quad (3.16)$$

In this Thesis, the methods of double-exposure holography and time-averaged holography (discussed in sections 3.1.3 and 3.1.4, respectively) were used to investigate vibrations of the TMs.

3.1.3. Double-exposure holography

In optoelectronic holography [Pryputniewicz, 1996; Furlong and Pryputniewicz, 1998; Hulli et al., 2007] information (mechanical deformations or displacements) in double-exposure investigations is related to the optical path change which can be extracted from the interference pattern of object and reference beams having complex light fields F_o and F_r respectively as

$$F_o = A_o \exp[i(\phi_o + \theta_n)], \quad (3.17)$$

and

$$F_r = A_r \exp[i(\phi_r)]. \quad (3.18)$$

After the beam splitter and considering phase stepping, intensity I_n of the combined wavefronts as recorded by the n-th video frame can be described by

$$\begin{aligned} I_n &= (F_o + F_r)(F_o + F_r)^*, \\ &= \{A_o \exp[j(\phi_o + \theta_n)] + A_r \exp[j\phi_r]\} \{A_o \exp[-j(\phi_o + \theta_n)] + \\ &\quad A_r \exp[-j\phi_r]\}, \\ &= |A_o|^2 + |A_r|^2 + 2A_o A_r \cos[(\phi_o - \phi_r) + \Delta\theta_n], \end{aligned} \quad (3.19)$$

where A_o and A_r are the amplitudes of the object and reference beams, ϕ_o is the randomly varying phase of the object beam, ϕ_r is the phase of the reference beam, and $\Delta\theta$ is the known phase step introduced between the frames. To facilitate double-exposure investigations, the argument of the periodic term of Eq. 3.19 is modified to include the phase change due to deformations of the object of interest subjected to specific loading and boundary conditions. This phase change is characterized by the fringe locus function Ω as

$$\begin{aligned}\Omega(x, y) &= 2\pi n(x, y) = [\mathbf{K}_2(x, y) - \mathbf{K}_1(x, y)] \cdot \mathbf{L}(x, y) \\ &= \mathbf{K}(x, y) \cdot \mathbf{L}(x, y),\end{aligned}\tag{3.20}$$

where $\mathbf{n}(x, y)$ is the interferometric fringe order at the known (x, y) coordinates, \mathbf{K} is the sensitivity vector, and \mathbf{L} is the displacement vector. Therefore, the intensity from a deformed object can be described by the intensity distribution (I_n').

$$I_n' = I_o + I_r + 2A_o A_r \cos[\Delta\phi + \Omega + \Delta\theta_n],\tag{3.21}$$

where $\Delta\phi$ is the random phase difference between two fields; $\Delta\phi = \phi_o - \phi_r$, and I_o and I_r represent the intensities of the object and reference beams, respectively. In Eq. 3.21, I_o is assumed to remain constant and the (x, y) arguments are omitted for clarity. Since it is Ω which carries information pertaining to mechanical displacements and/or deformations, the optoelectronic holography's video processing algorithm eliminates $\Delta\phi$ from the argument of the periodic function of the intensity distributions given in Eqs 3.19 and 3.21 by sequentially recording four frames with an introduction of a 90° phase shift between each frame. By solving the two sets of four simultaneous equations yields an image which is intensity modulated by a periodic function with Ω as the argument.

The optoelectronic holography operates in either display or data mode [Furlong and Pryputniewicz, 1998]. In display mode, interference patterns are observed at video rate speed and are modulated by a cosinusoidal function of the form

$$8A_o A_r \cos\left(\frac{\Omega}{2}\right),\tag{3.22}$$

which is obtained by performing specific mathematical operations between frames acquired at the undeformed and deformed states, described by Eqs 3.19 and 3.21, respectively. This mode is used for adjusting the optoelectronic holography system

and for qualitative investigations. Data mode is used for performing quantitative investigations. In data mode, two images are generated: a cosinusoidal image,

$$D = 64A_o^2 A_r^2 \cos(\Omega) , \quad (3.23)$$

and a sinusoidal image,

$$N = 64A_o^2 A_r^2 \sin(\Omega) , \quad (3.24)$$

which are processed simultaneously to produce quantitative results by computing and displaying at video rates

$$\Omega = \tan^{-1} \left(\frac{N}{D} \right), \quad (3.25)$$

Because of the discontinuous nature of Eq. 3.25, recovery of the continuous spatial phase distributions $\Omega(x, y)$ requires the application of the phase unwrapping algorithms [Kreis, 2005; Vest, 1979; Furlong et al., 2008]. In the measurements presented in this Thesis, double-exposure mode of the optoelectronic holography was used for quantitative stroboscopic measurements.

3.1.4. Time-averaged holography

Time-averaged holography involves a single holographic recording of an object undergoing a cycle vibration being constructed. For performing time-averaged holography or modal analysis of object of interest using optoelectronic holography, it is necessary to take into consideration a time varying fringe-locus function $\Omega_t(x, y, t)$ which is related to sinusoidally vibrating object under investigation [Pryputniewicz, 1985, 1987, 1989]. For this case, the intensity distribution can be represented by using Eq. 3.21 as

$$\begin{aligned}
I_t(x, y, t) &= I_o(x, y) + I_r(x, y) \\
&+ \\
&2A_o(x, y)A_r(x, y)\cos[\Delta\phi(x, y) + \Omega_t(x, y, t) + \Delta\theta_n]. \quad (3.22)
\end{aligned}$$

Since the CCD camera registers average intensity at the video rate characterized by the period Δt , the intensity that is observed is

$$I(x, y) = \frac{1}{\Delta t} \int_t^{t+\Delta t} I_t(x, y, t) dt, \quad (3.23)$$

and using phase stepping, the resulting intensity distribution for the n -th frame is of the form

$$\begin{aligned}
I_{t_n}(x, y) &= I_o(x, y) + I_r(x, y) \\
&+ \\
&2A_o(x, y)A_r(x, y)\cos[\Delta\phi(x, y) + \Delta\theta_n]M[\Omega_t(x, y)], \quad (3.24)
\end{aligned}$$

where $M[\Omega_t(x, y)]$ is known as the characteristic function that modulates the interference of two fields due to the motion of the object.

Equation 3.24 has four unknowns $I_o(x, y)$, $I_r(x, y)$, whose amplitudes are $A_o(x, y)$ and $A_r(x, y)$ respectively, $\Delta\phi(x, y)$, and $\Omega_t(x, y)$. The OEH's video frame processing algorithm eliminates $\Delta\phi$ from the argument of the intensity function given by Eq. 3.24. The aim of the analysis is to determine $\Omega_t(x, y)$ which relates directly to displacements of the object.

In order to solve for $\Omega_t(x, y)$ of a vibrating object, four sequential frames are recorded with a 90° phase shift between each frame. This procedure can be shown by the following set of equations:

$$I_{t1} = I_t + I_r + 2A_oA_r \cos(\Delta\phi_t + 0^\circ) M(\Omega_t), \quad (3.25)$$

$$I_{t2} = I_t + I_r + 2A_oA_r \cos(\Delta\phi_t + 90^\circ) M(\Omega_t), \quad (3.26)$$

$$I_{t3} = I_t + I_r - 2A_o A_r \cos(\Delta\phi_t + 180^\circ) M(\Omega_t), \quad (3.27)$$

$$I_{t4} = I_t + I_r - 2A_o A_r \cos(\Delta\phi_t + 270^\circ) M(\Omega_t). \quad (3.28)$$

Evaluating Eqs 3.25 to 3.28 yields an image which has an intensity modulated by a periodic function with Ω as the argument.

For time-averaged holography, the OEH can work either in display or data modes. In the display mode, interference patterns are observed at video rate and are modulated by a function of the form

$$4A_o A_r |M(\Omega_t)|. \quad (3.29)$$

This mode is used for adjusting the OEH system parameters and for qualitative investigations. These parameters include

- beam ratio, which must be characterized and set in order to maximize contrast and to avoid optical saturation of the CCD camera, can be calculated as

$$Br = avg \left[\frac{I_r(x,y)}{I_o(x,y)} \right].$$

It is suggested that the beam ratio for holographic interferometry is 1:1, but can be increased if it is necessary to reduce the exposure time [Vest, 1979].

- phase step θ_n obtained by calibration and used to acquire accurate intensity patterns $I_{t_n}(x, y)$.

The data mode is used to process the images quantitatively. In the data mode, additional images of the form

$$16I_o I_r [M^2(\Omega_t)], \quad (3.30)$$

are generated for quantitative processing and extraction of Ω_t .

Equations 3.29 and 3.30 indicate that the display and data images are proportional to the characteristic function and to the square root of characteristic

function, respectively. For the case of sinusoidal vibrations with a period much shorter than the video framing time, the characteristic function is determined by

$$M[\Omega_t(x, y)] = J_0[\Omega_t(x, y)], \quad (3.31)$$

where $J_0[\Omega_t(x, y)]$ is the zero order Bessel function of the first kind defining the location of centers of dark fringes seen during reconstruction.

4. IMPLEMENTATION OF OPTOELECTRONIC HOLOGRAPHIC OTOSCOPE SYSTEM

The OEHO system in this Thesis, which is used for full-field-of-view measurement of nanometer scale motions of TMs excited by sound in live human ears, is depicted in Fig. 4.1.

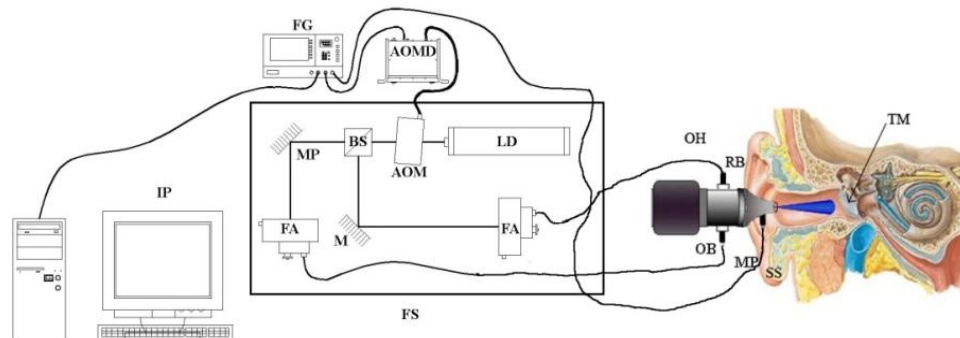


Fig. 4.1. Schematic of the OEHO system: TM is the sample under investigation; OH is the otoscope head containing an interferometer and imaging optics; FS is the fiber optic subsystem containing a laser, beam splitting optics, and laser-to-fiber components to provide an object beam (OB) and reference beam (RB); OH and FS are controlled by the image processing computer (IP). SS is the integrated sound source, and MP is the microphone. FG is the frequency generator which provides the timing input to the AOM driver (AOMD).

The developments from this project are based on optoelectronic methodologies that make use of miniaturized components in an otoscope configuration. The system consists of a high speed image processing computer (IP) with advanced control software, a fiber optic subsystem (FS), and an otoscope head subsystem (OH). Integrated in the otoscope head is a sound source (SS) and microphone (MP) to generate and measure sound stimuli under control of the IP. The OEHO system is capable of operating in time-averaged and double-exposure modes. The time-averaged mode is used for rapid identification of resonant frequencies and their

corresponding mode shapes of vibration in samples. Double-exposure mode is used for determination of the magnitude and phase of nanometer scale motions of the entire surface of the TMs between two states of deformation.

4.1 Fiber optic subsystem

The fiber optic subsystem (FS) used for transmission and modulation of laser light is shown in Fig. 4.2.

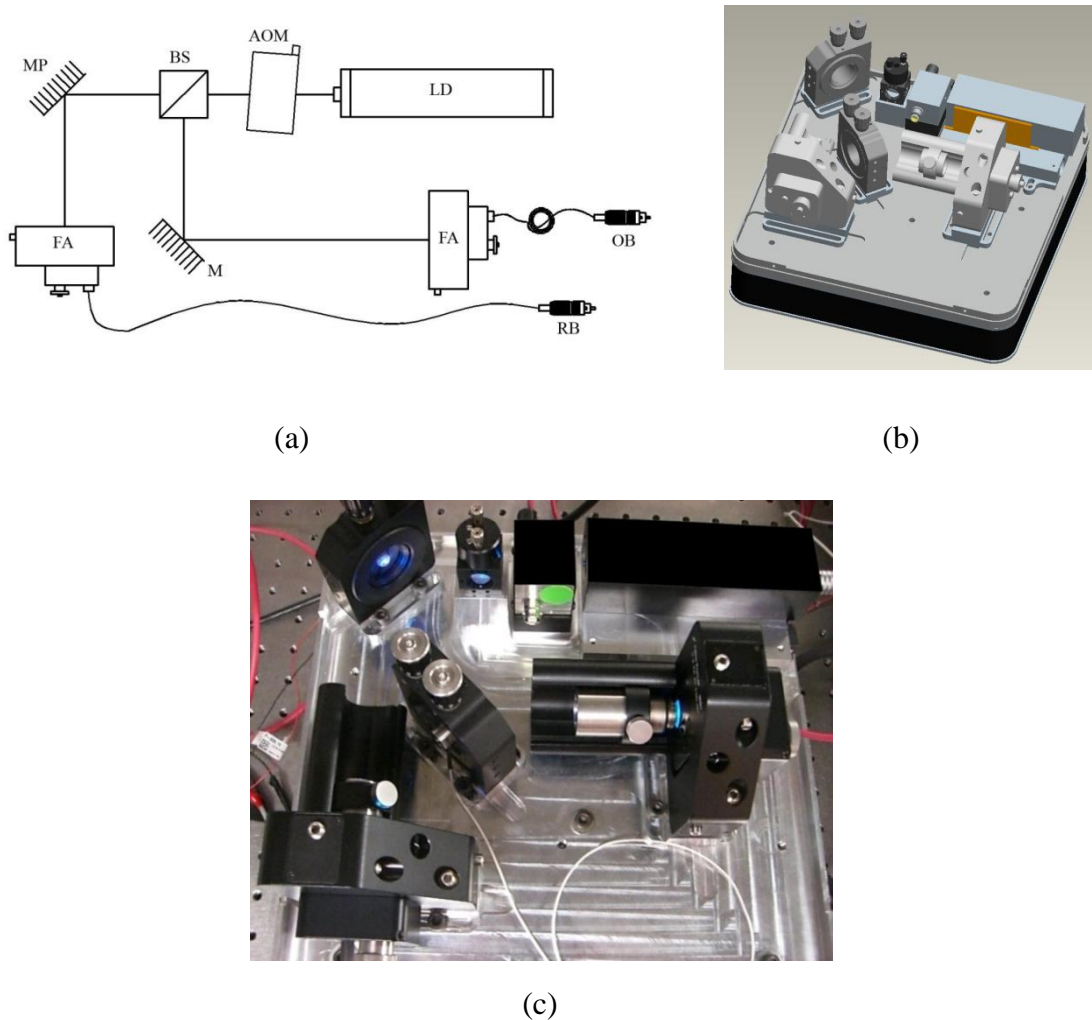


Fig. 4.2. Fiber optic subsystem: (a) schematic model depicting the major components; (b) CAD model depicting the major components; and (c) fabricated subsystem.

In biological samples, light interaction effects, such as reflection, refraction, and absorption, will diminish the quality of the fringes or contrast, which minimizes the accuracy of phase measurements. In order to overcome this, suitable methodologies that will allow improving the phase measurements through the enhancement of fringe contrasts were investigated. Different light sources, specifically different wavelengths and powers in combination with specific coating substances were based on nanoparticles were considered. For this Thesis the light source was chosen as a solid state laser (LD) with an operational wavelength of 473 nm and a power of 15 mW, and samples were coated with white paint.

As shown in Fig. 4.2a, the output of the laser is directed through an acousto-optic modulator (AOM) and through the beam splitter (BS), which splits the light into a reference beam (RB) and an object illumination beam (OB) with an 80:20 power ratio. The OB is directed to a mirror (M) and RB is directed to another mirror mounted onto piezoelectric modulators (MPM) to generate the required additional phase. Both beams are coupled into single mode fibers using laser-to-fiber coupler assemblies (FA).

4.2 Otoscope head subsystem

The optomechanical design was carried out with commercially available software [OSLO, 2005] as seen in Fig 4.3, by taking into account the TM anatomy and the results of preliminary holographic measurements of TM displacements in several animal species.

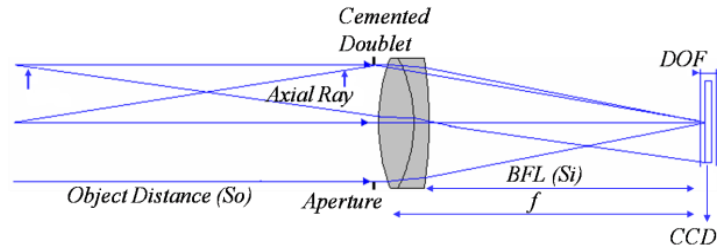


Fig. 4.3. Ray tracing using commercially available software. S_o : Object to front principal point distance, S_i : Rear principal point to image distance, DOF : Depth of field.

The OH subsystem houses a compact interferometer, a high speed CCD camera, and an imaging system (IS) which includes an achromatic lens and an aperture, and has characteristic dimensions of $100 \times 60 \times 120 \text{ mm}^3$.

Many innovative, accurate, and commercially available lens systems for use with cameras or the human eye have been designed as a result of research in optics. All the information collected by the system comes through the lens. In order to use a commercially available lens for the OEHO system, specific parameters of the lens were needed.

Commercially available lenses specify the lens focal length (f), the $F/\#$, which is a ratio between the lens focal length and diameter. With these two numbers we can calculate numerical aperture, field of view, and magnification of the image.

The numerical aperture is a dimensionless number, always less than 1, that describes the angular acceptance of rays of light in an optical element. The following equations define the relationship between $F/\#$, diameter (D_l) and focal length (f) [Hecht, 1989]:

$$F/\# = \frac{f}{D_l}, \quad (4.1)$$

$$F/\# = \frac{1}{2.NA}, \quad (4.2)$$

$$NA = \sin \theta, \quad (4.3)$$

$$\frac{1}{f} = \frac{1}{S_o} + \frac{1}{S_i}, \quad (4.4)$$

where NA and θ are the numerical aperture and the angle of incidence, respectively.

The correct lens selection can diminish image-processing requirements and improve system performance. The effects of a badly chosen lens cannot be corrected by software alone. The lens selection (correct lens focal length) is dependent on the field-of-view, pixel size of the CCD chip ($ps_{CCD} = 6.7 \times 6.7 \mu m^2$), region-of-interest ($ROI = 800 \times 800 \text{ pixels}$), magnification, and the object distance (S_o) of the system. The S_o is the distance from the lens to the object, which must be as short as possible (~90 mm) so that the system can be less expensive and more compact.

The required magnification (MAG) can be calculated by the ratio between the image size and the original dimensions of the object (~10 mm diameter for the TM), where the image size can be evaluated with the pixel size of the chip and ROI .

$$MAG = \frac{d_{image}}{d_{object}} = \frac{ps_{CCD} \cdot ROI}{d_{object}} = \frac{S_i}{S_o} \approx 0.5X. \quad (4.5)$$

Substituting Eq. (4.5) into Eq. (4.4), and solving for f , we get:

$$f = \frac{MAG}{MAG+1} \times S_o. \quad (4.6)$$

Therefore, we need a lens with focal length of approximately 30 mm. Figure 4.4 shows the schematic of the field of view calculation for the camera sensor with a $6.7 \mu m^2$ pixel size (ps_{CCD}), the object and an achromatic lens with f of 30 mm. Then FOV can be found as

$$FOV = 2 \cdot \arctan\left(\frac{d_{image}}{2 \cdot f}\right) \rightarrow 10 \text{ mm.} \quad (4.7)$$

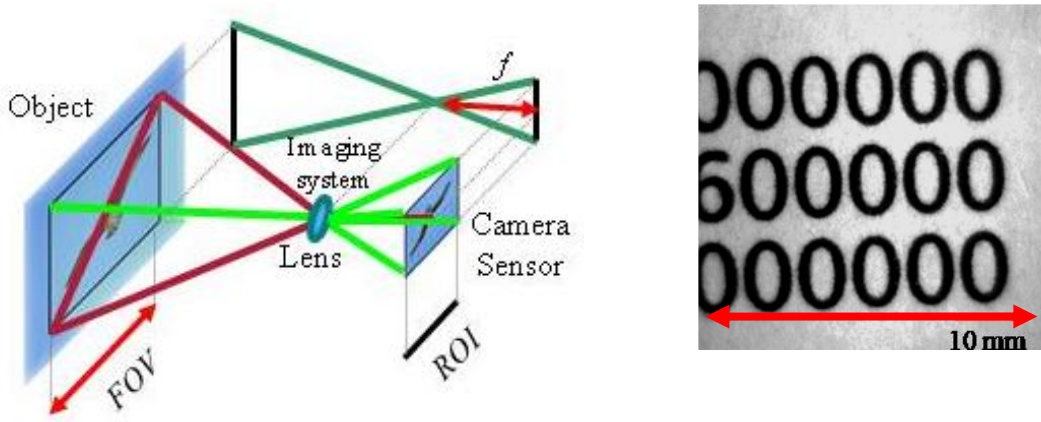


Fig. 4.4. Diagram of the imaging system: (a) parameters of the imaging system taken into account for the optical design. *FOV*: Field of view, *f*: Focal length, *ROI*: Region of interest, (b) target *FOV* of 10x10 mm².

To produce the optimal optical configuration, an assortment of lenses with various properties was tested, as shown in Table 4.1.

Table 4.1. Lenses tested.

Company	Part #	Lens type	Diameter (mm)	Focal length (mm)
Ross Optical	L-AOC315/110	Achromatic	21	40
Ross Optical	L-AOC129/110	Achromatic	18.5	31
OptoSigma	026-0450	Achromatic	20	30.60
Melles Griot	01LA0428	Achromatic	17.5	31
Melles Griot	01LA0783	Achromatic	25	25
THORLABS	AC127-019-A1	Achromatic	12.7	19

Table 4.1. Lenses tested. (*continued*)

THORLABS	AC127-025-A1	Achromatic	12.7	25
THORLABS	AC127-030-A1	Achromatic	12.7	30
THORLABS	AC127-050-A1	Achromatic	12.7	50
THORLABS	AC254-030-A1	Achromatic	25.4	30
THORLABS	AC254-035-A1	Achromatic	25.4	35
Edmund Optics	NT32-719	Achromatic	15	30
Edmund Optics	NT32-721	Achromatic	20	40
Lambda Research	PDA-19.1-030	Achromatic	19.1	30

Selecting the proper lens for the system requires making a number of choices such as lens shape, $F/\#$, distortion, anti reflection coating, and cost. Choosing the right lens type is important in minimizing optical aberrations.

Lens aberrations can be classified into two categories: chromatic and monochromatic. Chromatic aberrations are errors caused by color rays not traveling at the same velocity through the medium of the lens. The index of refraction of a lens material is a function of color. When using white light (that includes multiple ranges of colors), the different color frequencies are separated while passing through the lens and recombine at the focal length of the lens to form the image. Chromatic aberrations deteriorate the image by diminishing the contrast of the color in the image

[Hecht, 1987]. As seen in Table 4.1, THORLABS AC127-030-A1 achromatic lens, which is designed to limit the effect of lens aberrations, was chosen due to its dimensions, proper focal length and a better modulation transfer function (MTF), Fig. 4.5, which is a measurement of the lens' ability to transfer contrast from the object plane to the image plane at a specific resolution [Edmund Optics, Inc., 2006].

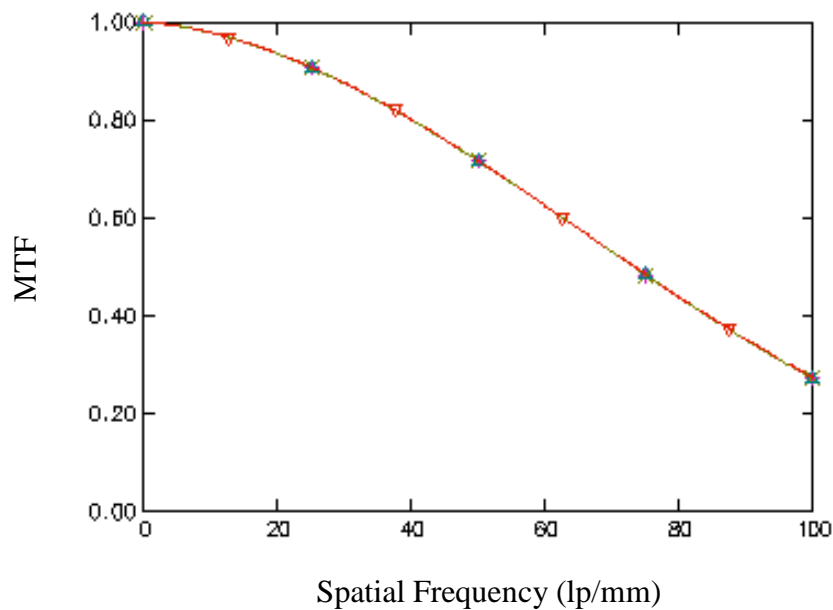


Fig. 4.5. MTF evaluated from OSLO software.

The Silicon Imaging SI-1280 monochrome CameraLink camera [Silicon Imaging, 2008] was selected as the camera in the OEHO for several important reasons. The required resolution of the project is 800x800 pixels: the camera's 1280 x 1024 sensor is sufficient for this and future higher resolutions if necessary. A 6.7 μ m pixel size gives the spatial resolution necessary for observing objects of

interest.

The camera's speed is only 30 frames per second at its full resolution, but offers higher frame rates when using a smaller region of interest. At the 800x800 resolution, the camera offers up to 80 frames per second which is sufficient for the project. As opposed to many cameras that only offer 8 or 10-bit image output, the SI-1280 offers up to 12-bit sampling, giving a much higher dynamic range than an 8 or 10-bit camera. Finally, the monochromatic version of the camera was selected because it is preferred for measurements of the laser beams in question.

A very important feature of this camera is its global shutter. As opposed to a rolling shutter, the global shutter takes a full-frame image. Since some of the aspects of this project (such as stroboscopic mode) require instantaneous capture, a rolling shutter would not be sufficient. Because a rolling shutter is more common, the global shutter was a major contributing factor into selecting the Silicon Imaging SI-1280 camera.

The aperture is used to limit the light entering the imaging system as well as to control the depth of field (*DOF*) for proper image focusing properties. Since lasers output such coherent beams of light, when this beam illuminates an object, the reflected light will interfere with itself as it is reflected off the surface of the object creating speckles. These speckles create a random intensity pattern in front of the object of interest and are highly fluctuating. If the aperture of the lens is decreased, the speckle size will increase. It was observed that the aperture diameter (D_a) should be at least 5 mm in diameter in order to minimize the speckle effect. In holographic interferometry, the speckles affect the achievable resolution and accuracy of the measurement; the size of each speckle is directly proportional to the laser's

wavelength,

$$d_{sp} = 1.22 \left(\frac{\lambda Si}{D_a} \right), \quad (4.6)$$

where D_a is the size of the aperture, Si is the image distance, and λ is the wavelength of the laser light.

The OH is enabled with a miniaturized sound source for sample excitation and a compact microphone for measurements of sound pressure. The sound source is driven by a frequency generator and the acoustic pressure is recorded with a data acquisition system.

As shown in Fig. 4.6a, the object illumination beam was coupled to the test object via a speculum (S). An angled glass window at the back of the speculum isolates the sound stimulus within the speculum, allowing larger stimulus sound pressures at lower frequencies. The output of the OB is used to illuminate the sample of interest while the imaging system (IS) collects the scattered wavefront from the surface of the samples, the TMs. The image formed by the IS is combined with the RB by means of the imaging beam splitter (BSI), and directed onto the CCD of the camera.

Based on the optical design parameters and the synthesized optomechanical configuration, the OH was fabricated, as shown in Fig. 4.6c. Its optical and imaging properties are as follows: field-of-view (FOV) of 10 mm^2 ; depth-of-field (DOF) of 5 mm; and magnification of 0.5X.

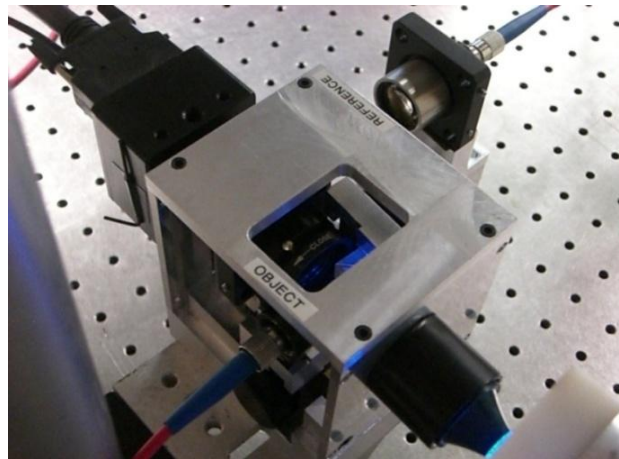
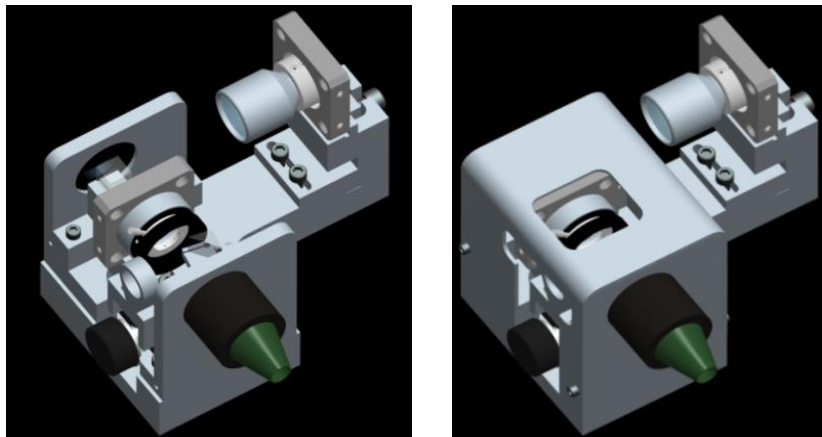
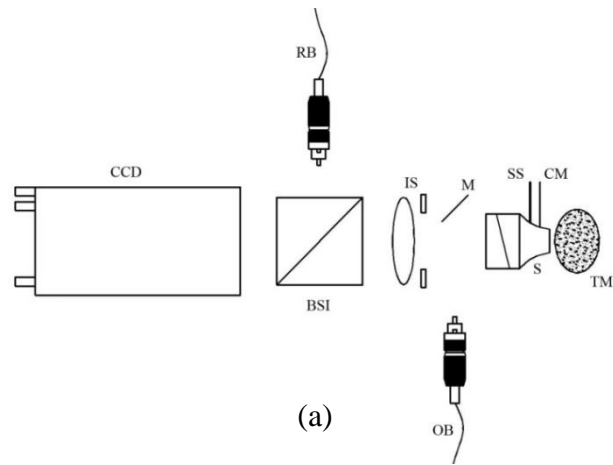


Fig. 4.6. Otoscope head subsystem: (a) schematic model depicting the major components; (b) CAD models depicting the major components; and (c) fabricated subsystem.

The system resolution was tested with a negative 1951 US Air Force (USAF) glass target by Edmund Optics because of its surface quality and maximum resolution (group 7, element 6, i.e. 228lp/mm). Here, negative indicates inversion of the background and bar colors. Figure 4.7 shows an example of a positive and a negative target. In the case of a negative target, the bar sets are openings, so the illumination must come from behind the target in order for the observation system to capture an image.

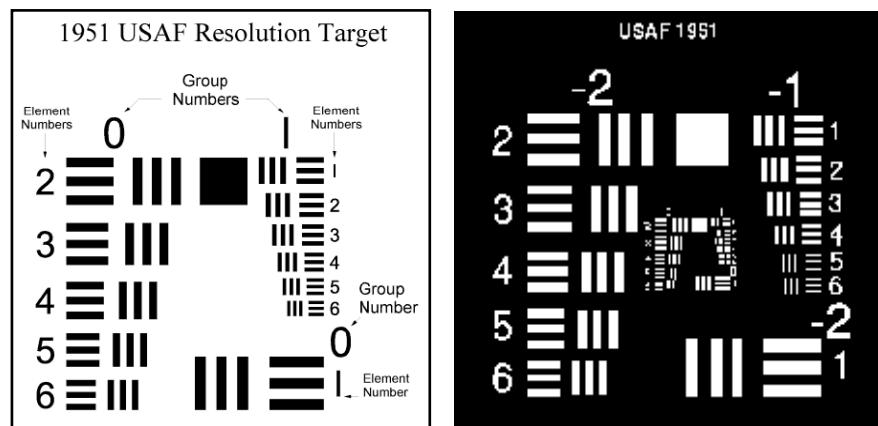


Fig. 4.7. USAF 1951 positive and negative target pattern [Edmund Optics, Inc., 2006].

The target is separated into groups and elements. Each element within a group corresponds to specific line pair (a set of a black line and a white line) per millimeter. The specification table of the target can be seen in Fig. 4.8.

Number of Line Pairs / mm in USAF Resolving Power Test Target 1951										
Group Number										
Element	-2	-1	0	1	2	3	4	5	6	7
1	0.250	0.500	1.00	2.00	4.00	8.00	16.00	32.0	64.0	128.0
2	0.280	0.561	1.12	2.24	4.49	8.98	17.95	36.0	71.8	144.0
3	0.315	0.630	1.26	2.52	5.04	10.10	20.16	40.3	80.6	161.0
4	0.353	0.707	1.41	2.83	5.66	11.30	22.62	45.3	90.5	181.0
5	0.397	0.793	1.59	3.17	6.35	12.70	25.39	50.8	102.0	203.0
6	0.445	0.891	1.78	3.56	7.13	14.30	28.50	57.0	114.0	228.0

Image Format - 1/4 to 228 line pairs/mm Target

Fig. 4.8. Specification table for the USAF resolution target [Edmund Optics, Inc., 2006].

Each group consists of six elements, which are progressively smaller by

$$l_l = \frac{2.5\text{mm}}{2^{Group + (Element - 1)/6}} \quad (4.7)$$

where l_l is the line length in millimeters for a given group and element [Glynn, 2002].

To get the resolution (the smallest feature that can be resolved by the imaging system) of the OH subsystem from the chart above, the negative 1951 USAF target was recorded as depicted in Fig. 4.9.

Since the smallest line pair that we can be distinguished is element 6 from group 5 that corresponds to 57.0 lp/mm (see Fig. 4.9), where the resolution of the imaging system is $17 \mu\text{m}$ (1 over 57.0).

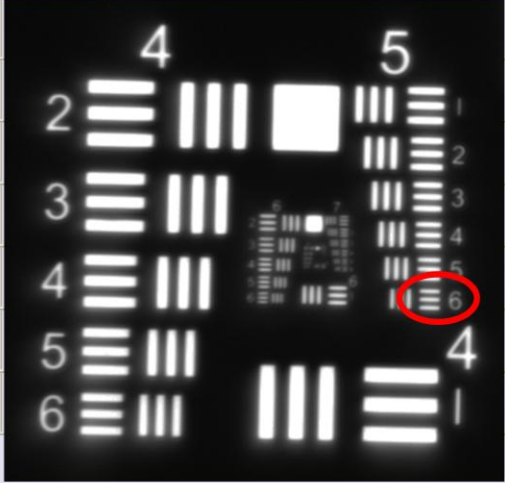
Number of Line Pairs / mm in USAF Resolving Power Test Target 1951						
Group Number						
Element		3	4	5	6	7
1		8.00	16.00	32.0	64.0	128.0
2		8.98	17.95	36.0	71.8	144.0
3		10.10	20.16	40.3	80.6	161.0
4		11.30	22.62	45.3	90.5	181.0
5		12.70	25.39	50.8	102.0	203.0
6		14.30	28.50	57.0	114.0	228.0
		pairs/mm Target				

Fig. 4.9. Recorded USAF 1951 negative glass target with group 5 outlined for containing the smallest resolvable element set [Edmund Optics, Inc., 2006].

The contrast ratio (C) of the full-field-of-view image is calculated as

$$C = \frac{I_{max} - I_{min}}{I_{max} + I_{min}}, \quad (4.8)$$

where I_{max} and I_{min} are the maximum and minimum interferogram intensity values respectively. Of the various techniques to find the contrast of an image, the line profile method, based on the intensity distribution of a line, is used in this investigation. Though this technique can be performed to calculate contrast in an image having random intensity profile, it is more reliable when used to calculate the contrast of a known pattern, such as the USAF target. As explained before, the USAF target has a sets of black and white lines that corresponds to a square wave profile having perfect contrast ($C = 1$) for different spatial frequencies.

Figure 4.10 demonstrates the line profile contrast calculation evaluated as 80.85%, indicating an excellent fringe contrast and, consequently high data quality. [Kreis, 2005]. Figure 4.10a shows an image of G4E2 with a line across the bar set, while Fig. 4.10b shows the intensity profile of the line and its corresponding contrast calculated numerically using MATLAB [MatLab 7.0, 2008].

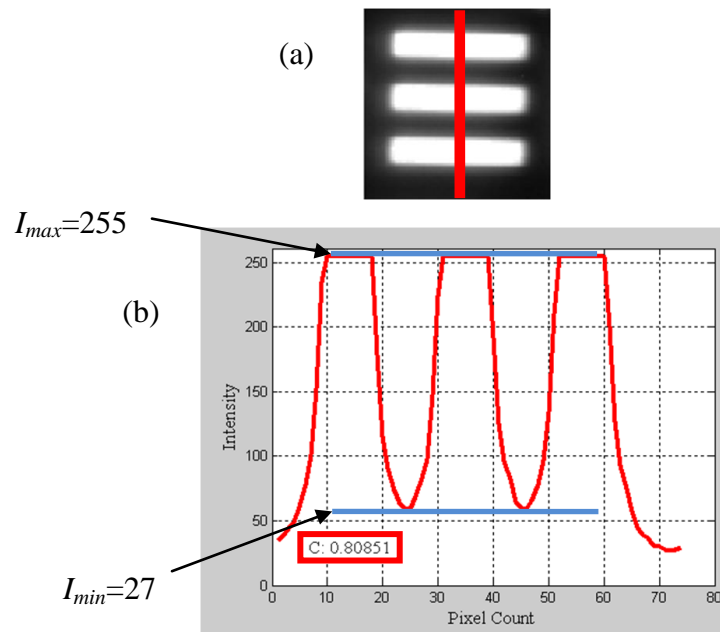


Fig. 4.10. Line profile contrast calculation method (a) image of G4E2 showing a line profile, (b) line intensity profile and contrast calculation.

Like the body sizes of different species of animals, the tympanic membrane of various species also varies in size. Different fields-of-view are necessary to accommodate these varying sizes. Therefore, the placement of the optics inside an enclosure has to allow for a range of working distances for fields of view of varying sizes. These limiting distances ultimately define the maximum allowable size of the enclosure, as shown in Table 4.2.

Table 4.2. Working distance constraints.

Image distance <i>Si</i> (mm)	Object distance <i>So</i> (mm)	Field of View <i>FOV</i> (mm)
29.7	96.2	11.2
30.4	89.8	10.0
34.3	78.9	8.5
38.9	69.9	6.7

5. EVALUATION OF THE OPTOELECTRONIC HOLOGRAPHIC OTOSCOPE SYSTEM

In order to evaluate the performance of the OEHO system, it was necessary that the device gathered images that were in fact representative of what was occurring at the time the image was recorded. To do so, a known geometry with predictable characteristics was essential to compare and draw conclusions with the experimental results that were obtained.

Because the geometry of the tympanic membrane is extremely complicated, it was simplified to a thin circular copper foil (membrane) with a thickness of 0.0254 mm and a diameter of 10 mm. A commercially available sample has the advantage over machined stock in that the thickness is very precise and the surface finish is consistent.

The membrane was secured on a piezoelectric shaker for sample excitation, Fig. 5.1, in a way that ensured uniform boundary conditions which resembled those in the analytical and computational modes.

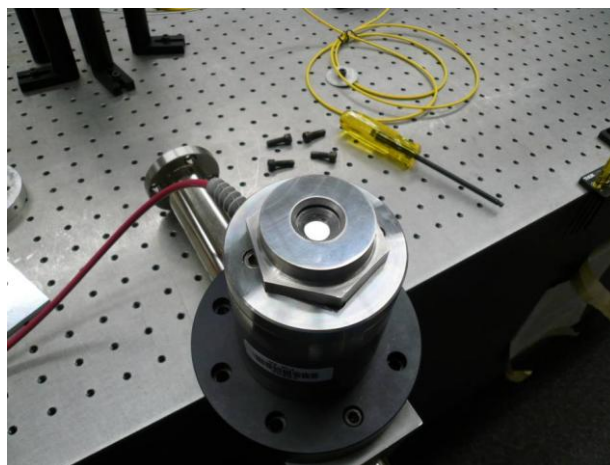


Fig. 5.1. A coated copper foil mounted on to the piezoelectric shaker.

To secure the foil (membrane) to the piezoelectric shaker, a device had to be designed and built in steel such a way that the foil could be clamped down between two surfaces. The base, in order to promote excitation was connected to the piezo. This provided the surface that the foil was laid on. The top part with a 10 mm hole in the middle is then placed on the foil.

The membrane was investigated with the OH subsystem set at the designed magnification of 0.5X, *FOV* of 10 mm, and a region of interest, *ROI*, of 800 x 800 pixels. In order to maximize contrast the sample was coated with white paint and the beam ratio between RB and OB was chosen to be ~ 1.2.

With the OEHO system running in the time-averaged mode and the membrane excited in the range of 2-8 kHz, fundamental natural frequencies were identified as depicted in Fig. 5.2 (see p.41). The frequency, starting with an amplitude of 10 volts, was continuously increased from 100 Hz until the first mode of vibration was reached. The amplitude was adjusted in order that the deformations were in the range of the OEHO system. Table 5.1 shows the data acquired for the first 6 modes of vibration of the copper foil membrane. Analysis of the interferograms indicates contrast of 0.80, which is suitable for quantitative analysis.

Table 5.1. Membrane test data.

Material	Thickness (mm)	Coating
Copper	0.0254	White Paint
Modes of vibration	Frequency (Hz)	Amplitude (Volts)
1	2150	5.4
2	4100	7.7
3	4470	2.7
4	6600	2.8
5	6630	2.7
6	7290	2.3

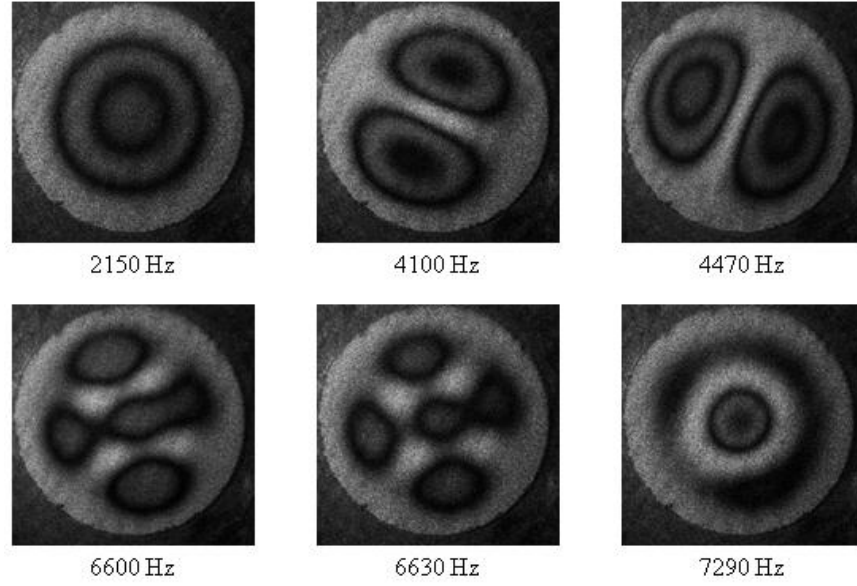


Fig. 5.2. Time-averaged interferograms of a test copper sample.

5.1. Analytical results

For the purpose of understanding the patterns within the Fig. 5.2, an analytical model of a circular, homogeneous, isotropic plate (membrane), undergoing free vibration which is clamped at the edges was developed. In this section, all of the following assumptions and equations (Eq. (5.1) through Eq. (5.16)) were compiled from derivations contained in the references McLachlan [1961] and Reddy [1999].

The equation of motion of an isotropic plate can be described as

$$D\nabla^2\nabla^2W + \mathbf{k}W - P_i\omega^2W + R_i\omega^2\nabla^2W = 0 \quad (5.1)$$

where D is the flexural rigidity, \mathbf{k} is the elastic modulus of the plate. The circular frequency and the deformation equation of the plate are represented as ω , W , respectively. Also, P_i and R_i are the principal and rotary inertia of the plate in which the rotary inertia (R_i) contributes little to the fundamental frequency so it can be simplified from the equation of motion

$$(\nabla^4 - \beta^4)W = 0 \quad (5.2)$$

where

$$\beta^4 = \frac{P_i \omega^2 - k}{D} \quad (5.3)$$

Equation (5.2) can be factored and the solution can be achieved by superimposing the solutions of the equations indicated in Eq. (5.4)

$$\nabla^2 W_1 + \beta^2 W_1 = 0, \quad \text{and} \quad \nabla^2 W_2 + \beta^2 W_2 = 0. \quad (5.4)$$

The solution to Eq. (5.2) is in the form of Fourier series

$$W(r, \theta) = \sum_{n=0}^{\infty} W_n(r) \cos n\theta + \sum_{n=1}^{\infty} W_n^*(r) \sin n\theta. \quad (5.5)$$

By substituting Eq. (5.5) into Eq. (5.4) gives the following identical equations for W_{n1} and W_{n2} :

$$\frac{d^2 W_{n1}}{dr^2} + \frac{1}{r} \frac{dW_{n1}}{dr} - \left(\frac{n^2}{r^2} - \beta^2 \right) W_{n1} = 0 \quad (5.6)$$

and

$$\frac{d^2 W_{n2}}{dr^2} + \frac{1}{r} \frac{dW_{n2}}{dr} - \left(\frac{n^2}{r^2} - \beta^2 \right) W_{n2} = 0 \quad (5.7)$$

Both Eqs (5.6) and (5.7) are in the form of Bessel's equation and have the solutions as

$$\begin{aligned} W_{n1} &= A_n J_n(\beta r) + B_n Y_n(\beta r) \quad \text{and,} \\ W_{n2} &= C_n Z_n(\beta r) + D_n K_n(\beta r) \end{aligned} \quad (5.8)$$

where J_n and Y_n are Bessel functions of the first and second kind respectively, and correspondingly, Z_n and K_n are the modified Bessel functions of the first and second kind. A_n , B_n , C_n , and D_n are the coefficients used to determine the mode shapes by applying the boundary conditions.

Hence, the general solution of Eq. (5.2) is

$$W(r, \theta) = \quad (5.9)$$

$$\begin{aligned} & \sum_{n=0}^{\infty} \{A_n J_n(\beta r) + B_n Y_n(\beta r) + C_n Z_n(\beta r) + D_n K_n(\beta r)\} \cos n\theta \\ & + \\ & \sum_{n=1}^{\infty} \{A_n^* J_n(\beta r) + B_n^* Y_n(\beta r) + C_n^* Z_n(\beta r) + D_n^* K_n(\beta r)\} \sin n\theta \end{aligned}$$

For solid circular plate, the terms including the modified Bessel functions, Y_n and K_n , are neglected as they would result in infinite values of deflection at the center of the membrane. Additionally, assuming that the solution is symmetric, any terms containing $\sin n\theta$ are neglected as well. This results in the following equation as the n th term of Eq. (5.9):

$$W_n(r, \theta) = \{A_n J_n(\beta r) + C_n Z_n(\beta r)\} \cos n\theta. \quad (5.10)$$

The boundary conditions for a clamped circular plate can be considered as

$$W_n = 0 \quad \text{and} \quad \frac{\partial W_n}{\partial r} = 0 \quad \text{at } r = a \text{ for any } \theta \quad (5.11)$$

and applying these boundary conditions to Eq. (5.10) we obtain

$$\begin{bmatrix} J_n(\gamma) & Z_n(\gamma) \\ J_n'(\gamma) & Z_n'(\gamma) \end{bmatrix} \begin{bmatrix} A_n \\ C_n \end{bmatrix} = \begin{bmatrix} 0 \\ 0 \end{bmatrix} \quad (5.12)$$

where $\gamma = \beta r$ evaluated at $r = a$ and the prime represents differentiation with respect to βr . Setting the determinant of the coefficient matrix in Eq. (5.12) to zero yields the following which is called the frequency equation

$$J_n(\gamma)Z_{n+1}(\gamma) + Z_n(\gamma)J_{n+1}(\gamma) = 0 \quad (5.13)$$

The roots γ can be approximated by using the asymptotic series for the Bessel functions as

$$\gamma_{n,m} \sim \theta - \frac{4n^2-1}{8\theta} \left[1 + \frac{1}{\theta} + \frac{28n^2+17}{48\theta^2} + \frac{3(4n^2-1)}{8\theta^3} + \frac{83n^4+54.5n^2+161.19}{120\theta^4} + \dots \right] \quad (5.14)$$

where $\theta = \frac{(2m+n)\pi}{2}$ for $m \geq 1$, m is the rank of the root and n is the order of the root.

Now, looking back at the definition of β in Eqn. (5.3), simple algebra can be used to develop an equation for determining the frequencies:

$$\omega^2 = \frac{D\beta^4 + k}{P_i} \quad (5.15)$$

Assuming that the membrane foundation is rigid $k = 0$ and substituting β with γ/a results in the final equation for determining the frequency of vibration

$$\omega = \frac{\lambda^2}{a^2} \sqrt{\frac{D}{P_i}} \quad (5.16)$$

Moreover, by applying specific shape functions to the derived equations, the shapes of the desired mode can be predicted as illustrated in Fig. 5.3. For a detailed representation of the MathCAD file used to generate these frequencies, refer to [Dwyer et al., 2008].

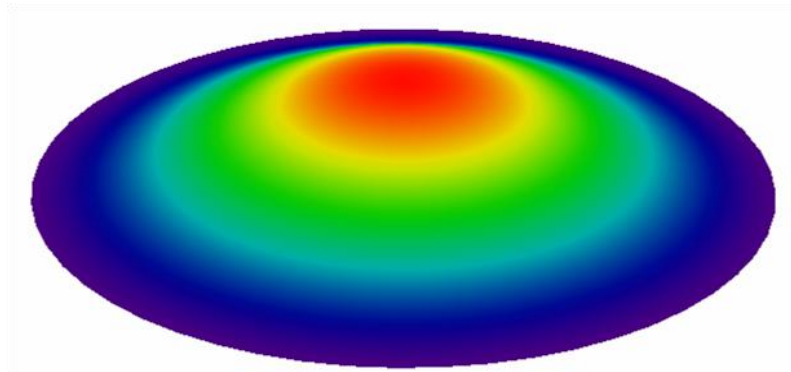


Fig. 5.3. First mode of vibration obtained with MathCAD [Dwyer et al., 2008].

5.2. Computational results

The finite element method (FEM) was used to solve the problem of verifying the consistency of the experimental results of an oscillating circular membrane. The

finite element program, Abaqus/CAE version 6.7 was used to model the oscillating membrane [Dwyer et al., 2008].

A 3D deformable solid with a diameter of 10 mm and a thickness of 0.0254 mm was made of the membrane. The material property of the copper with a density of 8960kg/m³, a Young's Modulus of 110 GPa and a Poisson's ratio of 0.343. A solid, homogeneous section was created and assigned to the entire membrane. A boundary condition was placed on the circumference of the membrane constraining movement in the x, y and z directions.

Results were obtained for the first six modes of vibration as shown in Fig. 5.4. A deformed contour plot on each of these six modes was created. Both the frequency and the shape of each individual mode were used to validate the data which had been obtained from the experimental and computational methods.

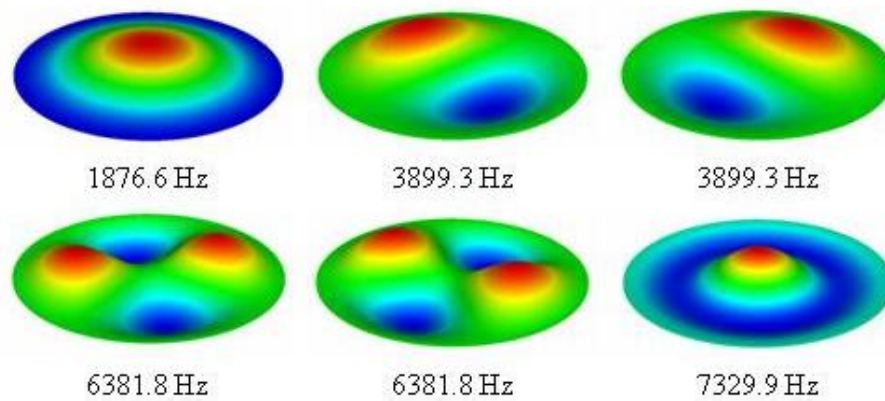


Fig. 5.4. Finite element method results for natural frequencies of a test copper sample [Dwyer et al., 2008].

5.3. Results comparisons

The analytical, computational, and experimental solutions (ACES) methodologies were used to validate the OEHO system [Pryputniewicz, 1994-b]. All methods provided the shapes and frequencies for the first six modes of vibration can be seen in Table 5.2.

Table 5.2. First six mode shapes and frequencies provided with ACES methodology [Dwyer et al., 2008].

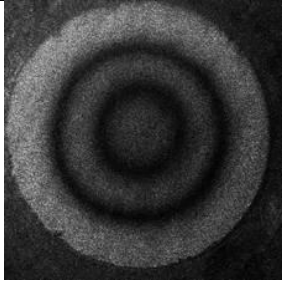
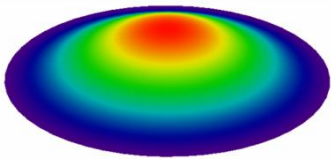
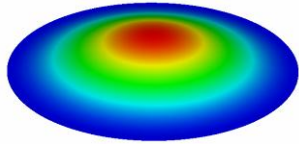
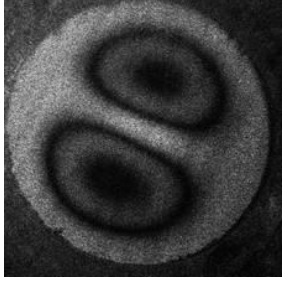
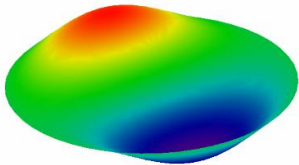
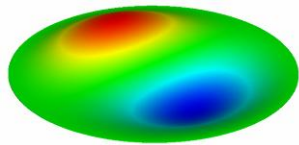
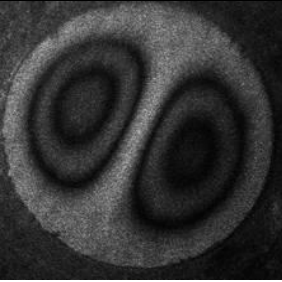
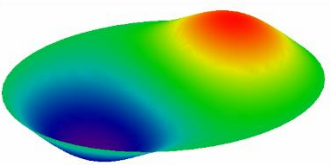
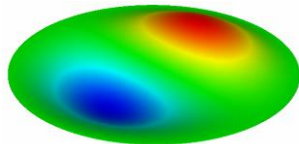
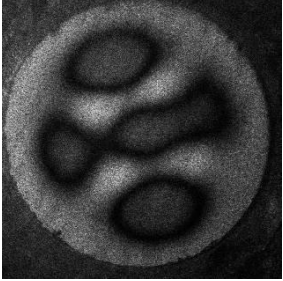
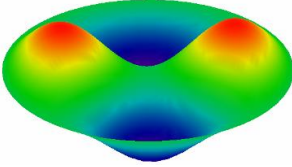
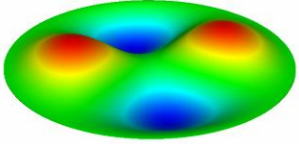
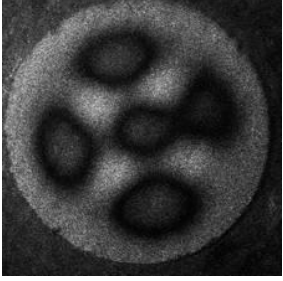
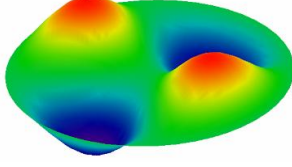
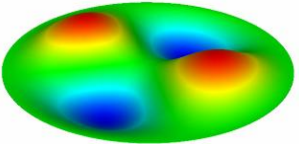
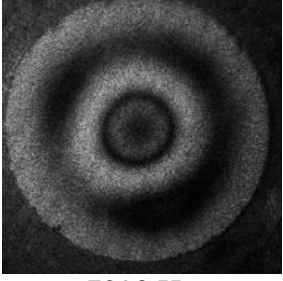
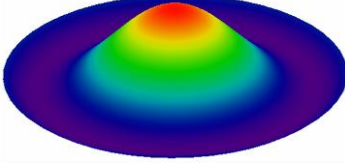
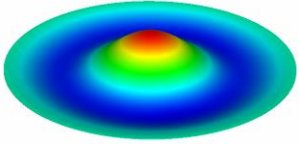
Mode	Experimental Results	Analytical Results	Computational Result
<u>Membrane Properties</u>	<u>Copper foil :</u> <ul style="list-style-type: none"> • 0.0254 mm thick, • 10 mm diameter, • coated with white paint. 	<u>Copper membrane clamped at the edges</u>	<u>Deformable solid circular membrane:</u> <ul style="list-style-type: none"> • 0.0254 mm thick • 10 mm diameter • 8960kg/m³ density
1	 <p>2150 Hz</p>	 <p>1830.6 Hz</p>	 <p>1876.6 Hz</p>
2	 <p>4100Hz</p>	 <p>3812.2 Hz</p>	 <p>3899.3 Hz</p>
3	 <p>4470 Hz</p>	 <p>3812.2 Hz</p>	 <p>3899.3 Hz</p>

Table 5.2. First six mode shapes and frequencies provided with ACES methodology [Dwyer et al., 2008]. (continued)

Mode	Experimental Results	Analytical Results	Computational Result
<u>Membrane Properties</u>	<u>Copper foil :</u> <ul style="list-style-type: none"> • 0.0254 mm thick, • 10 mm diameter, • coated with white paint. 	<u>Copper membrane clamped at the edges</u>	<u>Deformable solid circular membrane:</u> <ul style="list-style-type: none"> • 0.0254 mm thick • 10 mm diameter • 8960kg/m³ density
4	 <p>6600 Hz</p>	 <p>6256.3 Hz</p>	 <p>6381.8 Hz</p>
5	 <p>6630 Hz</p>	 <p>6256.3 Hz</p>	 <p>6381.8 Hz</p>
6	 <p>7290 Hz</p>	 <p>7128.6 Hz</p>	 <p>7329.9 Hz</p>

As demonstrated in Table 5.3, the error between the experimental, computational and analytical was calculated [Dwyer et al., 2008].

Table 5.3. Experimental result percent error [Dwyer et al., 2008].

Mode	Analytical Results	Computational Results
1	17.45%	14.57%
2	7.55%	5.15%
3	17.26%	14.64%
4	5.49%	3.42%
5	5.97%	3.89%
6	2.26%	0.54%

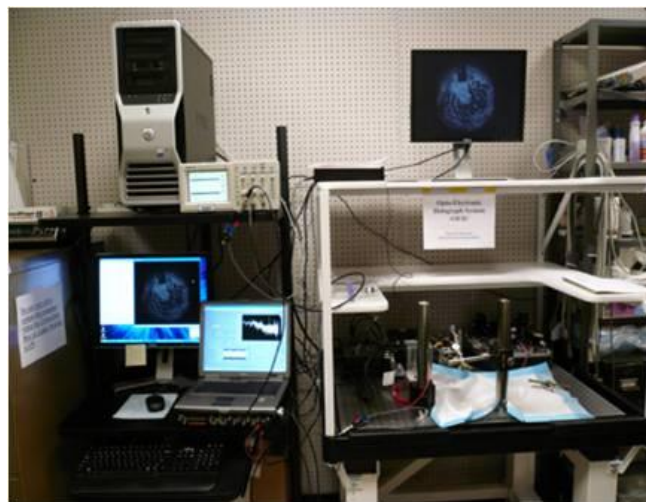
At most, the experimental results deviate from the analytical result by 17.45 percent for the first mode and 14.64 percent for the third mode from computational method.

Several sources can probably account for the error which occurred. First, both the analytical and computational models were greatly simplified. The force applied to the foil, which was assumed to be a thin cylindrical slice with a zero displacement boundary condition at the circumference, was ignored. The influence of the uneven pressure on the membrane was not taken into account while concluding the results. Furthermore, the paint on the membrane might also have been uneven as well as having added extra unaccounted mass to the membrane.

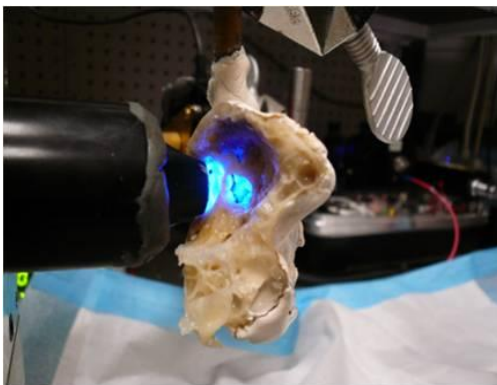
The error was minimized at higher modes with a minimum of 2.26 percent with the analytical method and 0.54 percent with the computational method. Even though there are some slight errors, the results indicate that the OEHO system was working as proposed.

6. OPTOELECTRONIC HOLOGRAPHIC OTOSCOPE SYSTEM IN MEDICAL ENVIRONMENT

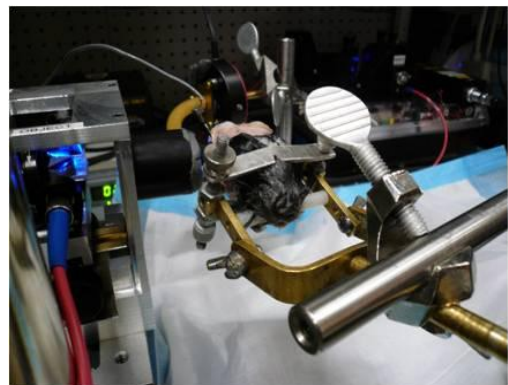
After the OEHO system was evaluated, it was deployed at the Massachusetts Eye and Ear Infirmary (MEEI) so that it could be used and evaluated under medical testing conditions for investigation and inspection of TMs, Fig.6.1.



(a)



(b)



(c)

Fig. 6.1. OEHO system installation: (a) OEHO system at MEEI; (b) otoscope head subsystem testing post mortem human temporal bone at MEEI; and (c) otoscope head subsystem testing post mortem chinchilla at MEEI.

6.1. Experimental results in tympanic membrane

In MEEI, both time-averaged holography and double-exposure holography measurements are being used and it has been observed that the OEHO system has a high mechanical stability while providing high quality images.

Several different sample types were prepared for use with the OEHO system. The test samples were acoustically excited using a speculum designed specifically to direct sound at the test samples. Figure 6.2 illustrates the time-averaged holography images of sound-induced TM displacements of a cadaveric human, a cadaveric chinchilla, live chinchilla and cadaveric cat, in the frequency range of 400 Hz to 25 kHz. The sound intensities, noted as dB SPL, were chosen to produce a moderate level of sound stimulation in each image.

At the top of each column is an illustration depicting the orientation of the exposed TM surface (the gray area). The frequency of excitation increases from top to bottom. The TM and manubrium are outlined in black, and the umbo is marked “U”. The thick horizontal line protruding from the top of the holograms of the chinchilla, and on the cat TM images there is the shadow of the probe tube used to measure the sound level of the stimulus.

Increasing displacements are indicated by the corresponding fringe densities. At frequencies less than 1 kHz, the TM displacement patterns are “simple”. These displacements are characterized by one or two regions of maximal displacement. These patterns are consistent with the previous results taken in 1972 from Tonndorf and Khanna [Tonndorf and Khanna, 1972]. At 4 kHz in cat and human, and near 1 kHz in the chinchilla, the TM displacement patterns are “complex,” and these

displacements are characterized by multiple regions of maximal displacement separated by areas of small displacement.

When the frequency is above 4 kHz in chinchilla and between 8 and 20 kHz in cat and human, the “ordered” patterns can be seen. These displacements are characterized by many small areas of maximal displacement around the manubrium.

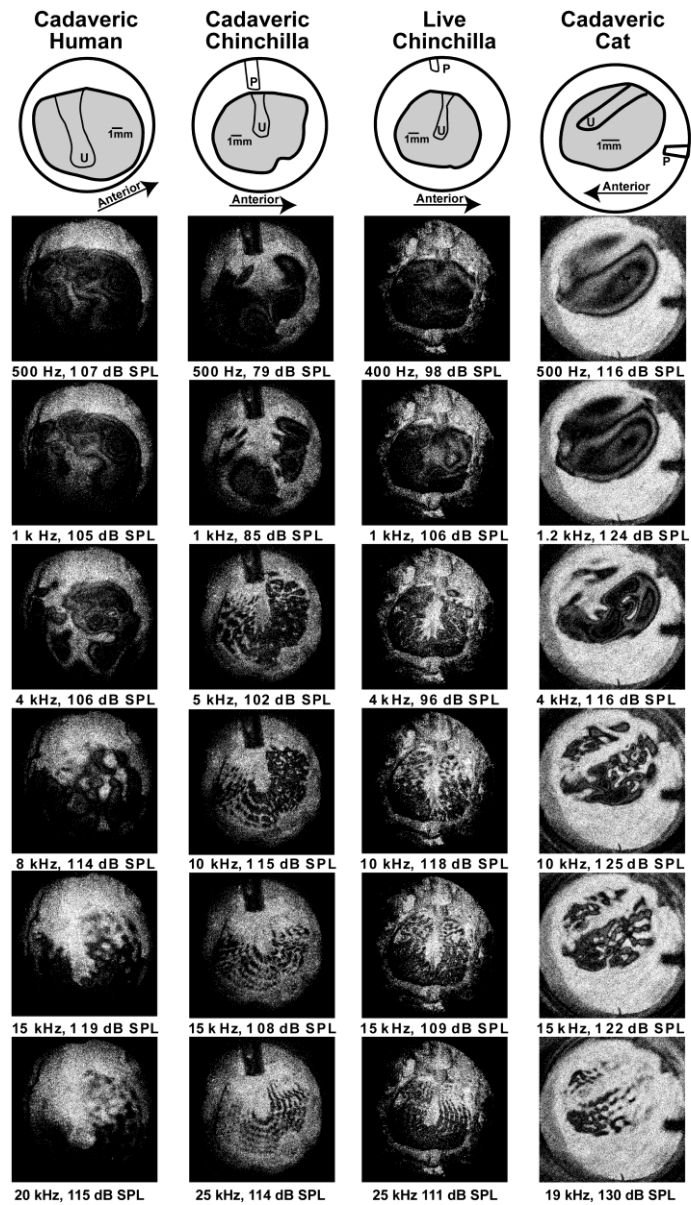


Fig. 6.2. Time-averaged holograms measured in cadaveric humans, in cadaveric chinchilla, in live chinchilla, and in cadaveric cat. The schematic on the top row shows the area of the TM in gray, location of the malleus, the umbo and the probe tube.

Double-exposure holography was used for quantitative measurements of the displacements of TM with nanometer resolution. With introducing stroboscopic illumination, any single hologram from the sample can be frozen at any point of its vibrating cycle by illuminating the object with short stroboscopic pulses, which can be adjusted with the duty cycle of the stroboscopic pulse (1/10 of the tonal excitation period), synchronized with the selected phase of the vibration excitation, Fig. 6.3. Stroboscopic illumination was obtained by means of an AOM placed in the laser beam before BS, see Fig. 4.1. Voltage pulses were applied to the AOM in synchrony with the sample excitation. These pulses were supplied by a frequency generator (FG) which permitted adjustment of the duty cycle of the stroboscopic pulse and its phase with respect to the tonal excitation.

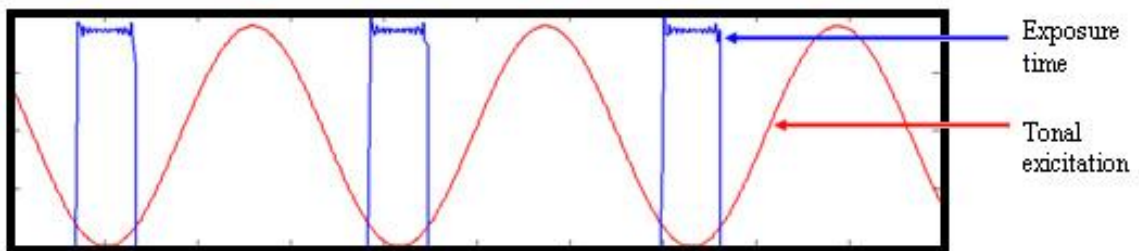
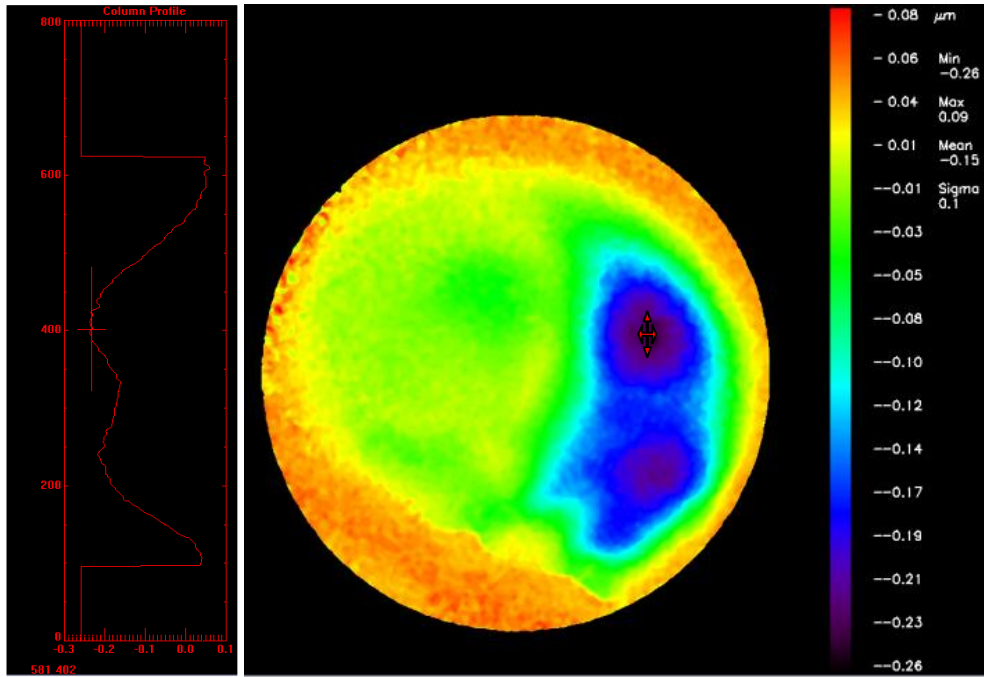


Fig. 6.3. Synchronization of the illumination with the object excitation.

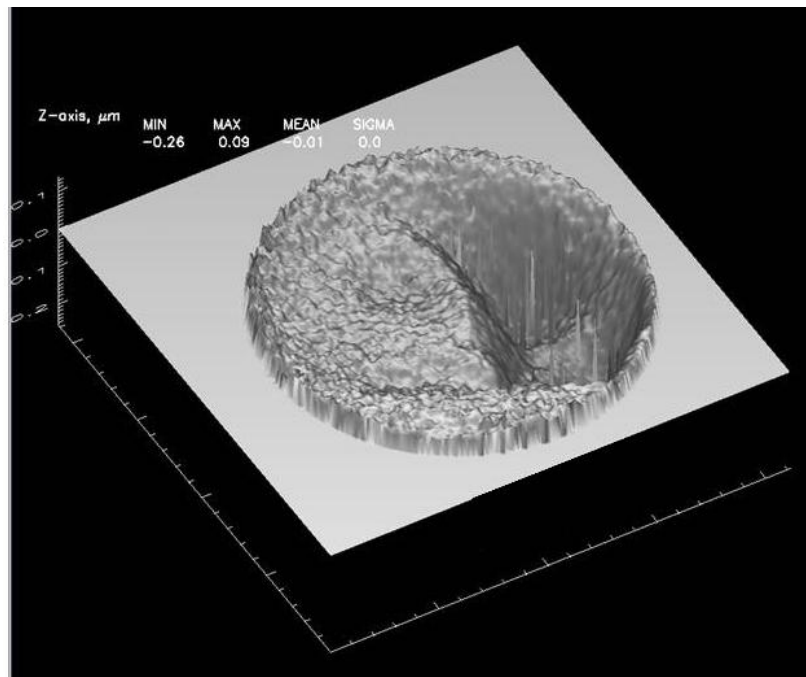
The holograms were processed using the phase stepping technique in order to extract the phase map depicting the sample displacement. Moreover, Figs 6.4, 6.5 and 6.6 show the difference in human temporal bone displacement between two stimulus

phase, both in 2D and 3D, at 500 Hz, 800 Hz, 4 kHz, 12 kHz, 15 kHz, and 20 kHz, respectively.

The colors changing between green and red code represents inward displacements of TM surface where as the colors varying between green and purple code is outward motions. The peak-to-peak surface out of plane displacement is on the order of 90nm, 120 nm, 190 nm, 150 nm, 210 nm, and 60 nm, respectively.

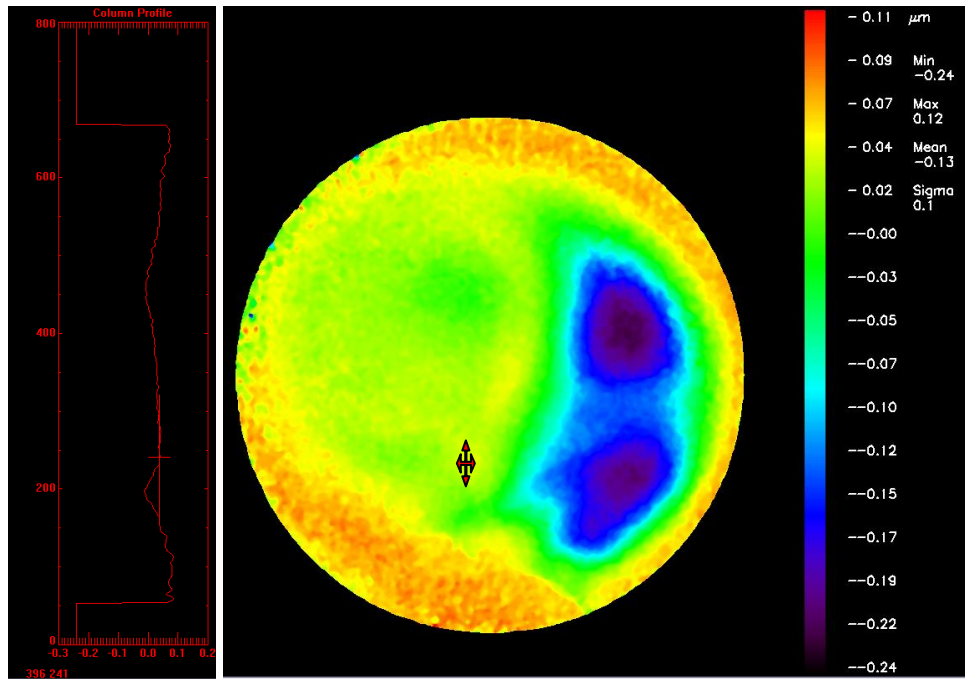


(a)

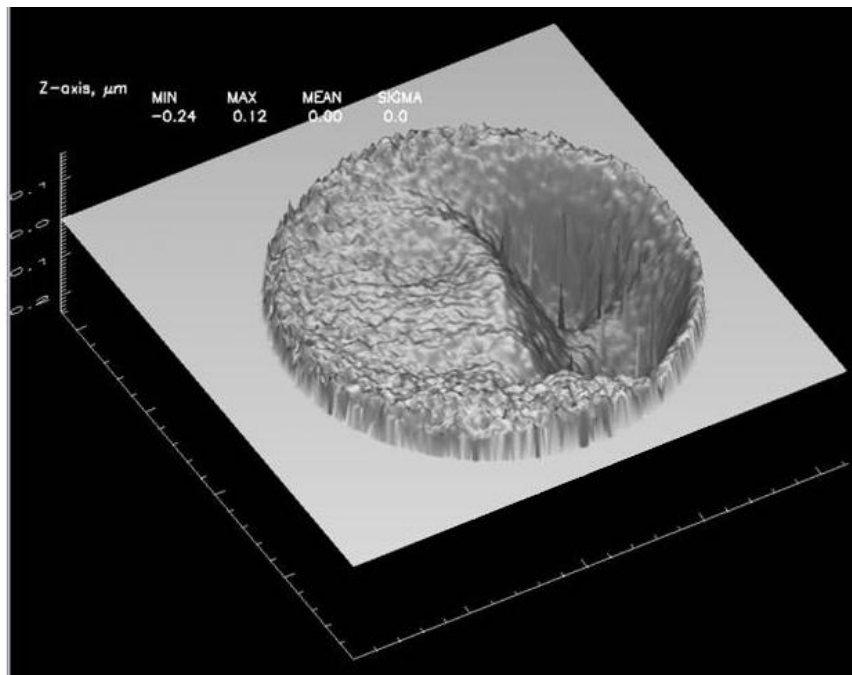


(b)

Fig. 6.4. Full-field-of-view stroboscopic holography measurements in human temporal bone at 500 Hz, showing a peak-to-peak surface out of plane displacement on the order of 90nm: (a) unwrapped phase (2D plot); and (b) 3D plot.

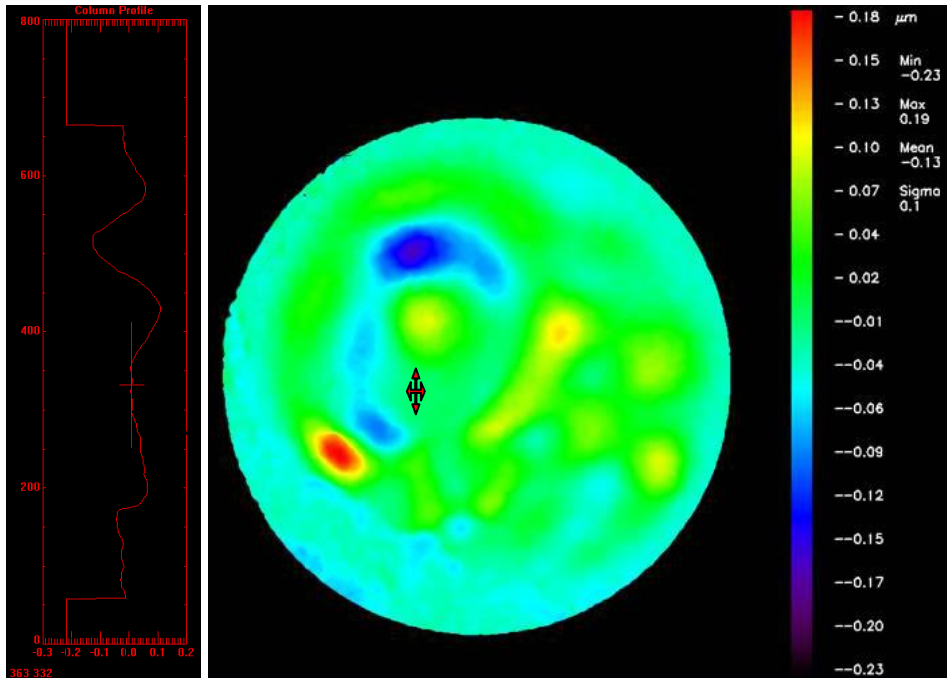


(a)

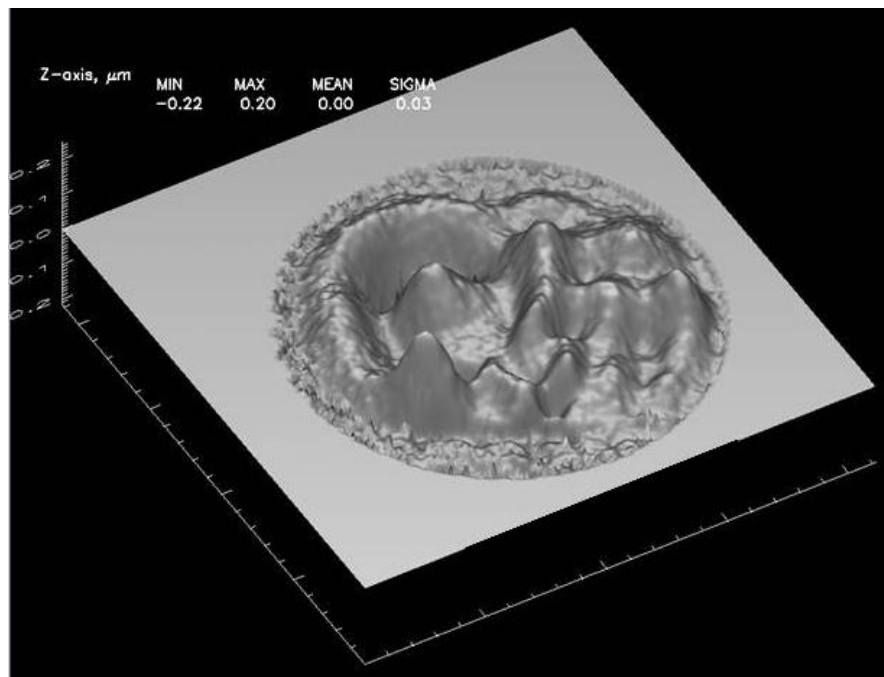


(b)

Fig. 6.5. Full-field-of-view stroboscopic holography measurements in human temporal bone at 800 Hz, showing a peak-to-peak surface out of plane displacement on the order of 120nm: (a) unwrapped phase (2D plot); and (b) 3D plot.

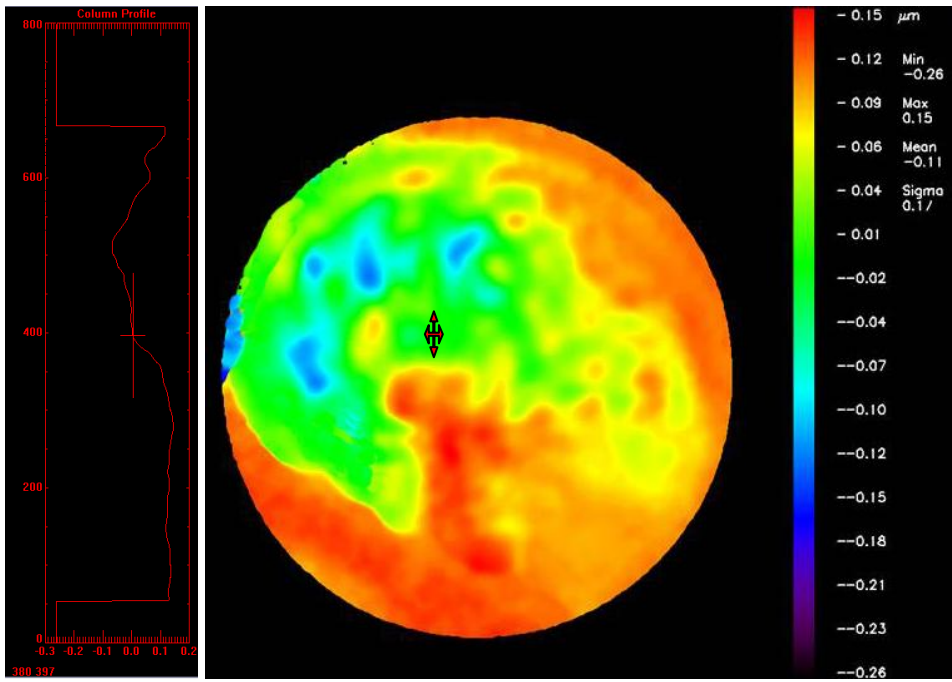


(a)

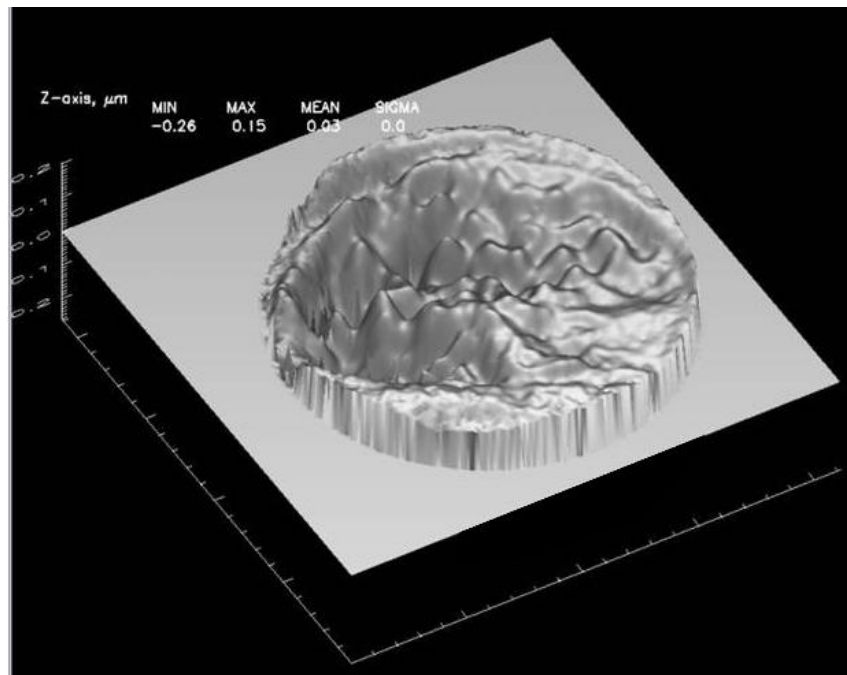


(b)

Fig. 6.6. Full-field-of-view stroboscopic holography measurements in human temporal bone at 4 kHz, showing a peak-to-peak surface out of plane displacement on the order of 190nm: (a) unwrapped phase (2D plot); and (b) 3D plot.

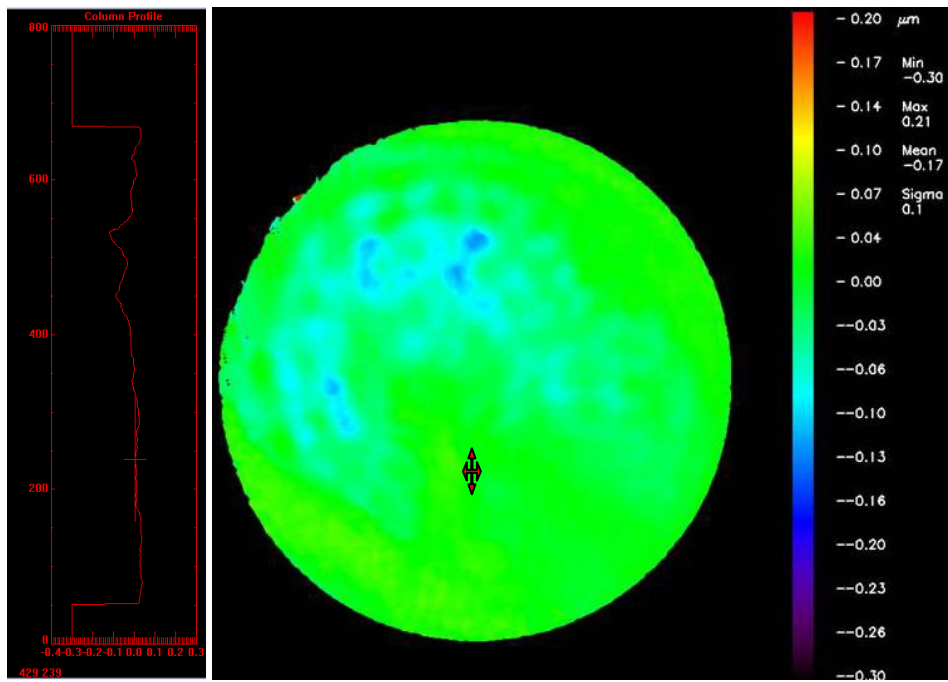


(a)

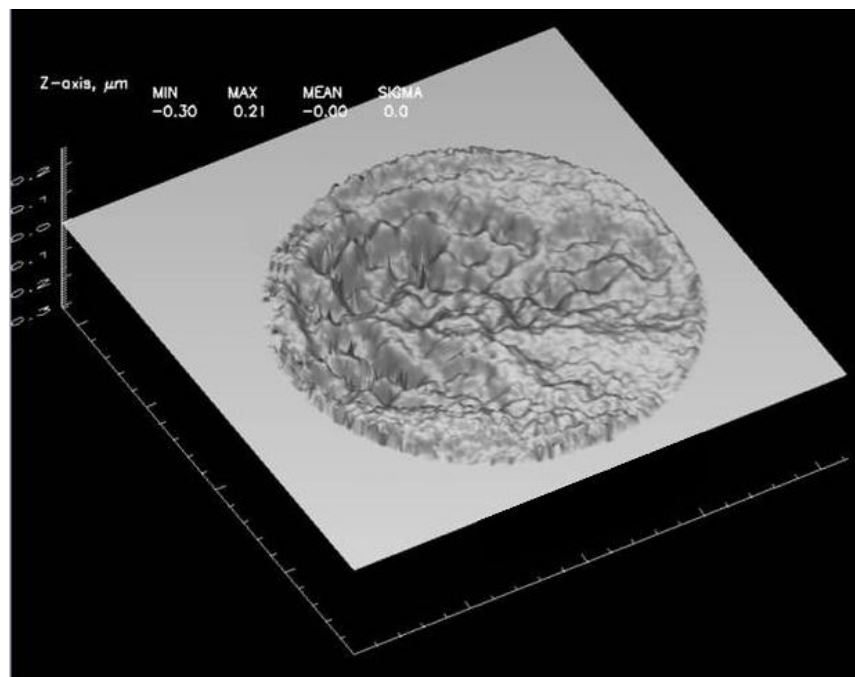


(b)

Fig. 6.7. Full-field-of-view stroboscopic holography measurements in human temporal bone at 12 kHz, showing a peak-to-peak surface out of plane displacement on the order of 150nm: (a) unwrapped phase (2D plot); and (b) 3D plot.

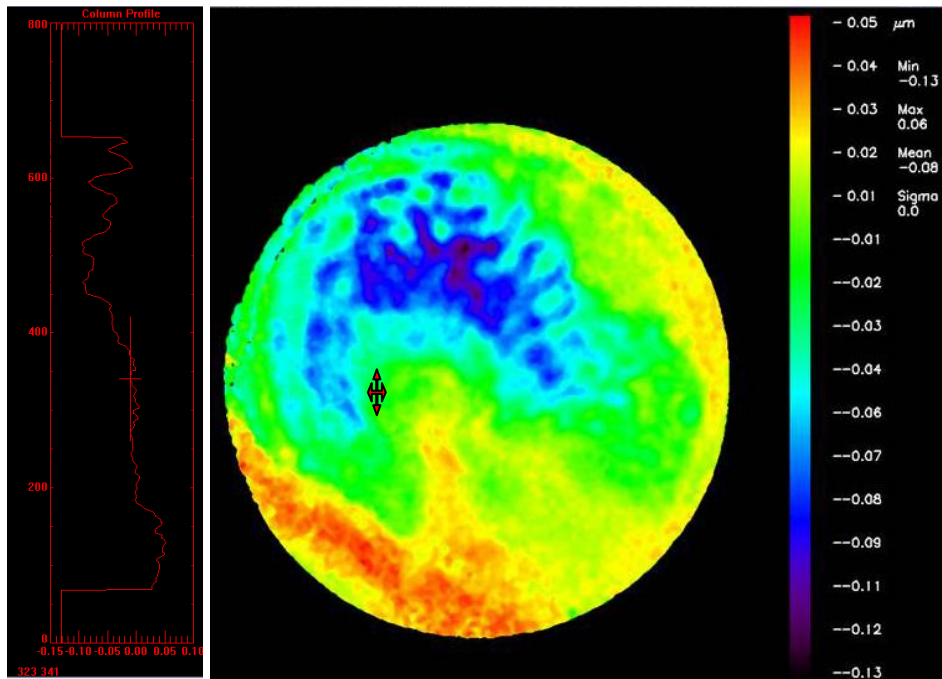


(a)

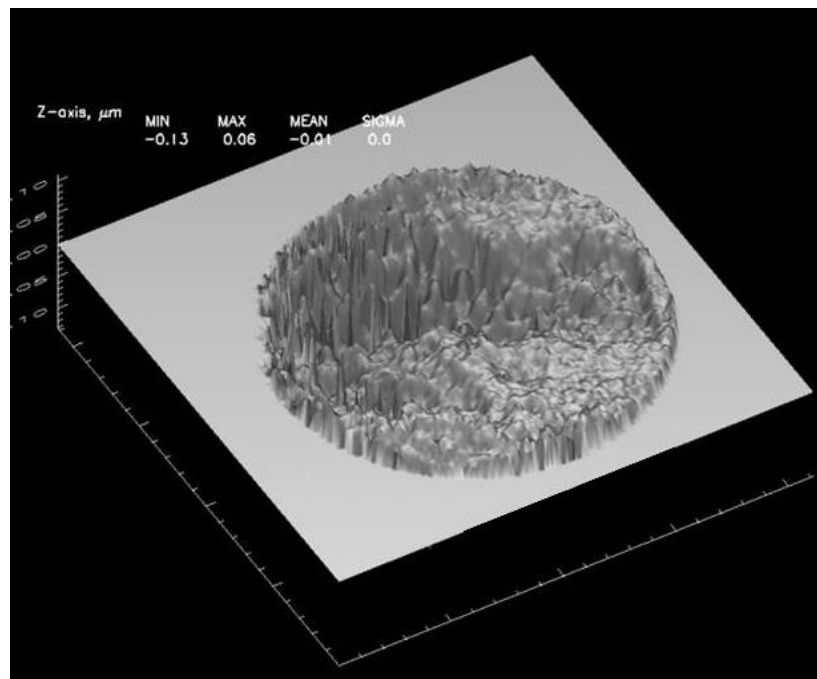


(b)

Fig. 6.8. Full-field-of-view stroboscopic holography measurements in human temporal bone at 15 kHz, showing a peak-to-peak surface out of plane displacement on the order of 210nm: (a) unwrapped phase (2D plot); and (b) 3D plot.



(a)



(b)

Fig. 6.9. Full-field-of-view stroboscopic holography measurements in human temporal bone at 20 kHz, showing a peak-to-peak surface out of plane displacement on the order of 60nm: (a) unwrapped phase (2D plot); and (b) 3D plot.

7. CONCLUSIONS AND FUTURE WORK

This Thesis has demonstrated the feasibility of the compact OEHO system for characterization of sound induced, nanometer scale deformations in the TM.

The OEHO system, operated in time-averaged and double-exposure modes, has been used to obtain measurements of TM behavior in three post mortem mammalian species: cat, chinchilla (including one live chinchilla) and human. Time-averaged holography used to determine the modes of vibration of all the species; double-exposure holography was applied to human temporal bone to obtain quantitative full-field-of-view measurements of deformations with nanometer resolution.

To illustrate measurement capabilities of the system, we have shown representative results of post-mortem and live chinchilla TM at frequencies of up to 25 kHz. The observed vibrations include simple, complex and ordered displacement patterns. However, the significance of this has yet to be understood.

The physiology of different species and the preliminary holographic measurements of TM motion were taken into account and dictated by the optomechanical parameters of the OEHO system. The following parameters characterize the OEHO configuration: *FOV* of 10 mm, *DOF* of 5 mm, *MAG* of 0.5X, *C* of 0.80 obtained with the beam ratio of 1.2 and resolution of 57.0 lp/mm.

The significance of the measurements presented demonstrates the applicability and validity of the OEHO systems. The most important fact was that the measurements, as presented, showed that the behavior of the TM had not been observed and quantified previously especially at such high frequencies.

Before being used in a medical research environment, a test was employed to evaluate the image quality and resolution by using finite element analysis, analytical and experimental solutions.

Further miniaturization of the OH subsystem by the use of MEMS technologies and advanced software tools for optomechanical design, analysis and manufacturing will continue. Challenges that are expected range from investigations on the fundamentals of laser-to tissue interaction, to improve and develop high-speed digital holographic algorithms.

Moreover, the OEHO system will be used to attempt answering fundamental questions related to the shape and function of the TM, the effects of middle-ear in hearing capabilities, the effects of perforations in TM, and the determination of mechanical properties of the TM.

8. REFERENCES

- Allen, J. B., Jeng, P. S., and Levitt, H., 2005, "Evaluation of human middle ear function via an acoustic power assessment," *JRRD*, 42(4):63-78.
- Castellini, P., Revel, G. M., and Tomasini, E. P., 1998, "Laser doppler vibrometry: A review of advances and applications," *The Shock and Vibration Digest*, 30(6):443-456.
- Castellini, P., Martarrelli, M., and Tomasini, E. P., 2006, "Laser doppler vibrometry: Development of advanced solutions answering to technology's needs," *Science Direct*, 20:1265-1285
- Csillag, A., 2005, *Atlas of the sensory organs: functional and clinical anatomy*, 1st ed., Human press, Totowa, New Jersey.
- Dwyer, B. W., Maccaferri, M. E., and Wester, C. R., 2008, *Design and realization of a laser holographic otoscope*, Department of Mechanical Engineering, Worcester Polytechnic Institute, Worcester, MA.
- Dirckx, J. J. J., and Decraemer, W. F., 2000, "Interferometer for eardrum shape measurement, based on projection of straight line rulings," *Lasers Med Sci*, 15:131-139.
- Edmund Optics, Inc., Edmund Optics, Inc., Barrington, NY, 2006.
- Fay, J., Puria, S., Decraemer, W. F., and Steele, C., 2005, "Three approaches for estimating the elastic modulus of the tympanic membrane," *J. Biomech.*, 38(9):1807-1815.
- Feeney, M.P., Grant, I. L., and Marryott, L.P., 2003, "Wideband energy reflectance in adults with middle-ear disorders," *J. Speech Lang. Hear. Res.*, 46:901-911.
- Fundamentals of hearing, http://www.mne.psu.edu/lamancusa/me458/2_hearing.pdf,

(last accessed: 19 August 2008).

- Funnell, W. R., and Laszlo, C. A., 1978, "Modeling of the cat eardrum as a thin shell using the finite-element method," *J. Acoust. Soc. Am.*, 63(5):1461-1467.
- Furlong, C., and Pryputniewicz, R. J., 1996, "Hybrid experimental and computational, investigation of mechanical components," *SPIE*, 2861:13-24.
- Furlong, C., and Pryputniewicz, R. J., 1998, "Hybrid computational and experimental approach for the study and optimization of mechanical components," *J. Opt. Eng.*, 37(5):1448-1455,
- Furlong, C., and Pryputniewicz, R. J., 1998, "Electro-optic holography method for determination of surface shape and deformation," *SPIE*, 3478:86-97.
- Furlong, C., Yokum, J. S., and Pryputniewicz, R. J., 2002, "Sensitivity, accuracy, and precision issues in opto-electronic holography based on fiber optics and high-spatial and high-digital resolution cameras," *Proc. Internat. Conf, on Measurements in Advanced Materials and Systems*, Milwaukee, WI.
- Furlong, C., Rosowski, J. J., Hulli, N., and Ravicz, M. E., 2007, "Preliminary analyses of tympanic-membrane motion from holographic measurements," *Proc. SEM, Selected Paper from the 8th ISMAN*.
- Furlong C., Hernández-Montes, M. S., Hulli, N., Cheng, J. T., Ravicz M. E., and Rosowski J. J., 2008, "Development of an optoelectronic holographic otoscope for characterization of sound-induced displacements in tympanic membranes," *31st Midwinter Meeting of the Association for Research in Otolaryngology*, Phoenix, Az.
- Furlong, C., Rosowski, J. J., Hulli, N., and, Ravicz, M., 2008, "Preliminary analyses of tympanic-membrane motion from holographic measurements," *Strain*, in-

press.

Glynn, E., "USAF and microscopy resolution test charts and pixel profiles,"

<http://www.efg2.com/Lab/ImageProcessing/TestTargets/>,

(last accessed: 20 November 2008)

Grundman, J., and Wigton, R., "Tympanic membrane evaluation", in *Ear*

Examination, <http://webmedia.unmc.edu/intmed/general/eye&ear/introtm.htm>,

(last accessed: 19 August 2008).

Hecht, E., 1989, *Optics*, 2nd ed., Addison-Wesley Publishing Company.

Hernández-Montes, M. S., Furlong, C., Rosowski, J. J., Hulli, N., and Harrington, E.,

2008, "Optoelectronic holographic otoscope for measurement of nano-displacements in tympanic membranes," *Proc. SEM*.

Holophile, Inc., "History of holography," <http://www.holophile.com/history.htm>,

(last accessed: 19 August 2008).

Huber, A. M., Schwab, C., Linder, T., Stoeckli, S. J., Ferrazzini, M., Diller N., and

Fisch U., 2001, "Evaluation of eardrum laser Doppler interferometry as a diagnostic tool," *Laryngoscope*, 111(3):501-507.

Hulli, N., Franco, R. A., Rodriguez-Vera, R., and Furlong, C., 2007, "Development of

an optoelectronic, high-speed, 3D shape measurement system for medical applications," *Proc. SEM*.

Katz, J., 1994, *Handbook of Clinical Audiology*, 4th ed., Williams & Wilkins,

Baltimore, Maryland.

Keefe, D. H., Bulen, J. C., Arehart, K. H., and Burns, E. M., 1993, "Ear-canal

impedance and reflection coefficient in human infants and adults," *J. Acoust. Soc. Am.*, 94(5):2617-2638.

- Khanna, S. M., and Tonndorf, J., 1972, "Tympanic membrane vibrations in cats studied by time-averaged holography," *J. Acoust. Soc. Am.*, 51(6): 1904-1920.
- Kreis, T., 2005, *Handbook of holographic interferometry*, Wiley-VCH, Weinheim, Germany.
- Kuypers, L. C., Decraemer, W. F., and Dirckx J. J. J, 2006, "Thickness distribution of fresh and preserved human eardrums measured with confocal microscopy," *Otol Neurotol*, 27(2): 256-264.
- Lim, D. J., 1970, "Human tympanic membrane, an ultrastructural observation," *Acta Otolaryngol.*, 70(3):176-186.
- Lim, D. J., 1995, "Structure and function of the tympanic membrane: a review," *Acta otorhinolaryngol. Belg.*, 49(2):101-115.
- Løkberg, O. J., Høgmonen, K., and Gundersen, T., 1980, "Vibration measurement of the human tympanic membrane – in vivo," *Acta Otolaryngol.*, 89(1-2):37-42.
- Margolis, R. H., Saly, G. L., and Keefe, D. H., 1999, "Wideband reflectance tympanometry in normal adults," *J. Acoust. Soc. Am.*, 106(1):265-280.
- McLachlan, N.W., 1961, *Bessel Functions for Engineers*, Oxford University Press, Amen House, London E.C.4.
- MatLab 7.0, The Mathworks, Natick, MA, 2008.
- Mikoklai, T. K., Duffey, J., and Adlin, D., "A guide to tympanometry for hearing," <http://www.maico-diagnostics.com/eprise/main/Maico/Products/Files/MI24/Guide.Tymp.pdf>, (last accessed: 19 August 2008).
- OSLO software for opto-mechanical modeling, Optics Reference , Lambda Research Corporation, Littleton MA, 2005.

- Pryputniewicz, R. J., and Stetson, K. A., 1980, "Determination of sensitivity vectors in hologram interferometry from two known rotations of the object," *Appl. Opt.*, 19:2201-2205
- Pryputniewicz, R. J., 1985, "Time average holography in vibration analysis," *Opt. Eng.*, 24(5):843-848.
- Pryputniewicz, R. J., 1987, "Quantitative interpretation of time-average holograms in vibration analysis," *Optical metrology*, in NATO Advanced Science Institute (ASI) Series, Porto, Portugal, pp. 296-371.
- Pryputniewicz, R. J., 1989, "Measurement of vibration patterns using electro-optic holography," *SPIE*, 1162:456-467
- Pryputniewicz, R. J., 1994-a, "Quantitative determination of displacements and strains from holograms," in *Holographic Interferometry*, P. K. Rastogi, ed., Springer-Verlag, Berlin, pp. 33-72.
- Pryputniewicz, R. J., 1994-b, "A hybrid approach to deformation analysis," *SPIE*, 2342:282-296.
- Pryputniewicz, R. J., 1996, *Holographic numerical analysis*, ME/CHSLT-NEST, Worcester Polytechnic Institute, Worcester, MA.
- Pryputniewicz, R. J., Yokum, J. S., and Furlong, C., 2002, "Optoelectronic holography method for measurements of absolute inside shapes of objects," *Proc. 2002 Internat. Conf. on Measurements in Advanced Materials and Systems, SEM, Milwaukee, WI.*
- Reddy, J.N., 1999 *Theory and Analysis of Elastic Plates*, Taylor & Francis, 325 Chestnut Street, Philadelphia, PA 19106.
- Robinson, D. W., and Reid, G. T., 1993, *Interferogram analysis, digital fringe pattern*

measurement techniques, 1st ed., Taylor & Francis, England, pp. 23-71.

Rosowski, J. J., Carney, L. H., Lynch, T. J., and Peake, W. T., 1986, "The effectiveness of external and middle ears in coupling acoustic power into the cochlea," in: *Peripheral Auditory Mechanisms*, Allen, J. B., Hall, J. L., Hubbard, A., Neely, S. T., and Tubis, A., eds, New York, Springer-Verlag, pp. 3-12.

Rosowski, J. J., 1996, "Models of external- and middle- ear function," in: *Auditory computation*, Hawkins, H. L., McMullen, T. A., Popper A. N., and Fay, R. R., eds, Springer-Verlag New York, Inc., NY, pp 15-60.

Rosowski, J. J., Nakajima, H. H., and Merchant, S. N., 2008, "Clinical utility of laser-doppler vibrometer measurements in live normal and pathologic human ears," *Ear & Hearing*, 29(1):3-19.

Sanna, M., Sunose H., Mancini, F., Russo, A., and Taibah, A., 2003, *Middle ear and mastoid microsurgery*, Georg Thieme Verlag, Stuttgart, Germany, pp.1-15.

Schubert, E. D., 1980 *Hearing: Its function and dysfunction*, Springer-Verlag, New York, NY.

Shanks, J. E., Lilly, D. J., Margolis, R. H., Wiley, T. L., and Wilson, R. H., 1988, "Tympanometry," *J. Speech and Hearing Disorders*, 53:354-377.

Silicon Imaging SI 1280F Mega Camera,

http://www.alacron.com/camera/machine%20vision%20cameras/Silicon%20Imaging/SI_Silicon%20imaging_SI-1280F.pdf, (last accessed: 19 November 2008).

Sundberg, M., 2008, *Optical methods for tympanic membrane characterization towards objective otoscopy in otitis media*, Department of Biomedical

Engineering, Linköpings universitet, Linköping Dissertation No. 1173,
Linköping, Sweden, pp.19-21.

Tonndorf, J., and Khanna, S. M., 1970, "The role of the tympanic membrane in middle ear transmission," *Ann. Otol. Rhinol. Laryngol.*, 79(4):743-753.

Tonndorf, J., and Khanna, S. M., 1971, "The tympanic membrane as a part of the middle ear transformer," *Acta Otolaryngol.*, 71(2):177-180.

Tonndorf, J., and Khanna, S. M., 1972, "Tympanic-membrane vibrations in human cadaver ears studied by time-averaged holography," *J. Acoust. Soc. Am.*, 52(4):1221-1233.

Vest, M. C., 1979, *Holographic Interferometry*, John Wiley & Sons.

Wada, H., Kobayashi, T., Suetake, M., and Tachizaki, H., 1989, "Dynamic behavior of the middle ear based on sweep frequency tympanometry," *Audiology.*, 28:127-134.

Wada, H., Ando, M., Takeuchi, M., Sugawara, H., and Koike, T., 2002, "Vibration measurement of the tympanic membrane of guinea pig temporal bones using time averaged speckle pattern interferometry," *J. Acoust. Soc. Am.*, 111(5):2189-2199.

Whittemore, K. R., Merchant, S. N., Poon B. B., and Rosowski, J. J., 2004, "A normative study of tympanic membrane motion in humans using a laser Doppler vibrometer (LDV)," *Hearing Research*, 187(1-2):85-104.

Wikipedia, <http://upload.wikimedia.org/wikipedia/commons/7/7c/HumanEar.jpg>,

(last accessed: 19 August 2008).

Appendix A - MATLAB code for line profile contrast calculation

```
% The program bellow reads an image, investigates the intensity
profile
% across the image. Calculates the contrast of a line profile
% Also, if the image is too small, the program can crop a
% desire portion of the image and scale it up.

% _____ %%% _____
% read, display, and calculate the profile of a line in the image
clear all
[file, path] = uigetfile('*.*','Select the image to be analyze:');

J = imread([path file]);

% [X,map] = rgb2ind(J,255);
% J = ind2gray(X,map);

figure('NumberTitle', 'off', 'Name', 'Profile of the image');
Jcrop = imcrop(J);

figure('NumberTitle', 'off', 'Name', 'Profile of the image');
Jresize = imresize(Jcrop,2);

% imagesc(Jresize), colormap(gray);
imshow(Jresize)

P1 = improfile;
%P2 = improfile;
%P3 = improfile;
%P4 = improfile;
%P5 = improfile;
%P6 = improfile;
%P7 = improfile;
%P8 = improfile;
%P9 = improfile;
%P10 = improfile;

% title(file)

% _____ %%% _____
% calculate contrast
Imax1 = max(P1);
Imin1 = min(P1);

C1 = (Imax1 - Imin1)/(Imax1 + Imin1);

Imax2 = max(P2);
Imin2 = min(P2);

C2 = (Imax2 - Imin2)/(Imax2 + Imin2);

Imax3 = max(P3);
Imin3 = min(P3);
```

```

C3 = (Imax3 - Imin3)/(Imax3 + Imin3);

Imax4 = max(P4);
Imin4 = min(P4);

C4 = (Imax4 - Imin4)/(Imax4 + Imin4);

Imax5 = max(P5);
Imin5 = min(P5);

C5 = (Imax5 - Imin5)/(Imax5 + Imin5);

Imax6 = max(P6);
Imin6 = min(P6);

C6 = (Imax6 - Imin6)/(Imax6 + Imin6);

Imax7 = max(P7);
Imin = min(P7);

C7 = (Imax7 - Imin7)/(Imax7 + Imin7);

Imax8 = max(P8);
Imin8 = min(P8);

C8 = (Imax8 - Imin8)/(Imax8 + Imin8);

Imax9 = max(P9);
Imin9 = min(P9);

C9 = (Imax9 - Imin9)/(Imax9 + Imin9);

Imax10 = max(P10);
Imin10 = min(P10);

C10 = (Imax10 - Imin10)/(Imax10 + Imin10);

Cavg = (C1 + C2 + C3)/3;

Cavg = (C1+C2+C3+C4+C5+C6+C7+C8+C9+C10)/10;

C = C1

% _____%%
close all

figure('NumberTitle', 'off', 'Name', 'Line profile average
contrast');
subplot(2,2,1)
% imshow(Jcrop)
imagesc(Jcrop), colormap(gray)
subplot(2,2,2)
plot(P1, '-r', 'linewidth', 1);
hold on
plot(P2, 'ob', 'linewidth', 1);
plot(P3, ':g', 'linewidth', 1);

```



```

hold off

xlabel('Pixel Count');
ylabel('Intensity');
ylim([0 260]);

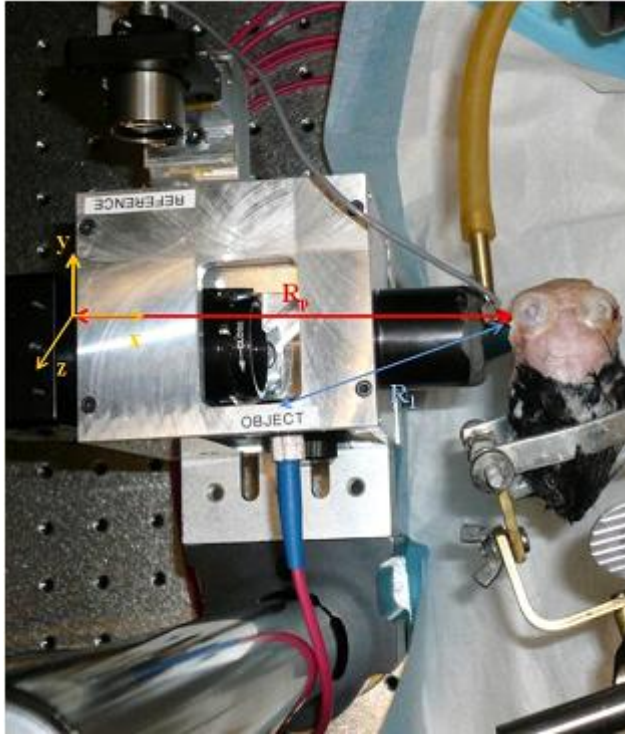
y = get(gca,'ylim'); mid = y(2)/2; del = y(2)/10 ;
x = get(gca,'xlim'); mid2 = x(2)/2; del2 = x(2)/10;
&text(mid2,mid,['C_l_p_a_v_g: ' num2str(Cavg)], ...
text(mid2,mid,['C: ' num2str(C)], ...
    'HorizontalAlignment', 'right', ...
    'BackgroundColor', 'white', 'linewidth',2) ;
grid on;

figure(3)
plot(P1, '-r', 'linewidth', 1);
y = get(gca,'ylim'); mid = y(2)/2; del = y(2)/10 ;
x = get(gca,'xlim'); mid2 = x(2)/2; del2 = x(2)/10;
text(mid2,mid,['C_l_p_a_v_g: ' num2str(Cavg)], ...
    'HorizontalAlignment', 'right', ...
    'BackgroundColor', 'white', 'linewidth',2) ;
grid on;

```

Appendix B - Matcad file for determining the sensitivity vector for OEHO system

Given:



$$\lambda := 0.47\mu\text{m}$$

μm

$$R_1 := (-21.01 \ 0 \ 58.8)$$

i, j, k vectors, mm

Position vector of illumination

$$R_2 := (0 \ 0 \ 0)$$

i, j, k vectors, mm

Position vector of observation

$$R_p := (0 \ 0 \ 112.02)$$

i, j, k vectors, mm

Position vector object

Solutions:

$$\text{den}_1 := \sqrt{\left(R_{p0,0} - R_{10,0}\right)^2 + \left(R_{p0,1} - R_{10,1}\right)^2 + \left(R_{p0,2} - R_{10,2}\right)^2}$$

$$\text{den}_1 = 57.217 \quad \text{mn}$$

$$\text{den}_2 := \sqrt{\left(R_{20,0} - R_{p0,0}\right)^2 + \left(R_{20,1} - R_{p0,1}\right)^2 + \left(R_{20,2} - R_{p0,2}\right)^2}$$

$$\text{den}_2 = 112.02 \quad \text{mn}$$

Unit vectors:

$$k_1 := \left(\frac{R_{p0,0} - R_{10,0}}{\text{den}_1} \quad \frac{R_{p0,1} - R_{10,1}}{\text{den}_1} \quad \frac{R_{p0,2} - R_{10,2}}{\text{den}_1} \right)$$

$$k_1 = (0.367 \ 0 \ 0.93)$$

Unit vector for the direction of illumination

$$k_1 = 0.367i + 0j + 0.93k$$

Unit vector form

$$k_2 := \left(\frac{R_{20,0} - R_{p0,0}}{\text{den}_2} \quad \frac{R_{20,1} - R_{p0,1}}{\text{den}_2} \quad \frac{R_{20,2} - R_{p0,2}}{\text{den}_2} \right)$$

$$k_2 = (0 \ 0 \ -1)$$

Unit vector for the direction of observation

$$k_2 = 0 \cdot i + 0 \cdot j - 1 \cdot k$$

Unit vector form

Magnitudes

$$K_{1\text{magnitude}} := \sqrt{\left(k_{10,0}\right)^2 + \left(k_{10,1}\right)^2 + \left(k_{10,2}\right)^2} \quad K_{1\text{magnitude}} = 1$$

$$K_{2\text{magnitude}} := \sqrt{\left(k_{20,0}\right)^2 + \left(k_{20,1}\right)^2 + \left(k_{20,2}\right)^2} \quad K_{2\text{magnitude}} = 1$$

Vectors

$$k := \frac{2 \cdot \pi}{\lambda} \quad k = 13.284 \quad \frac{1}{\mu\text{m}}$$

$$K_1 := k \cdot k_1 \quad K_1 = (4.878 \ 0 \ 12.356)$$

$$\boxed{K_1 = 4.878i + 0 \cdot j + 12.356k} \quad \frac{1}{\mu\text{m}} \quad \text{Illumination vector}$$

$$K_2 := k \cdot k_2 \quad K_2 = (0 \ 0 \ -13.284)$$

$$\boxed{K_2 = 0 \cdot i + 0 \cdot j - 13.284k} \quad \frac{1}{\mu\text{m}} \quad \text{Observation vector}$$

Given the three points, the illumination vector came out to be, K1, while the observation vector, K2. For both cases, the magnitudes resulted in 0. Using this results, the sensitivity vector can be calculated following the equation in the class notes.

$$K_{\text{ill}} := (4.878 \ 0 \ 12.356) \quad \frac{1}{\mu\text{m}} \quad \text{Illumination vector}$$

$$K_{\text{ob}} := (0 \ 0 \ -13.284) \quad \frac{1}{\mu\text{m}} \quad \text{Observation vector}$$

$$K_{\text{total}} := \left[\left(K_{\text{ob}_{0,0}} - K_{\text{ill}_{0,0}} \right) \left(K_{\text{ob}_{0,1}} - K_{\text{ill}_{0,1}} \right) \left(K_{\text{ob}_{0,2}} - K_{\text{ill}_{0,2}} \right) \right]$$

$$\boxed{K_{\text{total}} = (-4.878 \ 0 \ -25.64)} \quad \frac{1}{\mu\text{m}} \quad \text{Sensitivity vector}$$

Magnitude

$$K_{\text{total_mag}} := \sqrt{\left(K_{\text{total}_{0,0}} \right)^2 + \left(K_{\text{total}_{0,1}} \right)^2 + \left(K_{\text{total}_{0,2}} \right)^2}$$

$$K_{\text{total_mag}} = 26.1 \quad \frac{1}{\mu\text{m}}$$

Unit vector

$$K_{\text{total_unit}} := \begin{pmatrix} \frac{K_{\text{total}_{0,0}}}{K_{\text{total_mag}}} & \frac{K_{\text{total}_{0,1}}}{K_{\text{total_mag}}} & \frac{K_{\text{total}_{0,2}}}{K_{\text{total_mag}}} \end{pmatrix}$$

$$K_{\text{total_unit}} = (-0.187 \ 0 \ -0.982)$$

$$K_{\text{unit_mag}} := \sqrt{\left(K_{\text{total_unit}_{0,0}}\right)^2 + \left(K_{\text{total_unit}_{0,1}}\right)^2 + \left(K_{\text{total_unit}_{0,2}}\right)^2}$$

$$K_{\text{unit_mag}} = 1$$

The procedure above calculated the sensitivity vector the the points specified. The sensitivity vector has units of 1/length, as K1 and K2. The magnitude was calculated to be 26.1 1/μm. While the magnitude of its unit vector was 1, which is standard.